

1 **The Ice, Cloud, and land Elevation Satellite-2 (ICESat-2): Science requirements,**
2 **concept, and implementation**

3

4 Thorsten Markus¹, Tom Neumann¹, Anthony Martino¹, Waleed Abdalati², Kelly
5 Brunt^{1,3}, Beata Csatho⁴, Sinead Farrell³, Helen Fricker⁵, Alex Gardner⁶, David
6 Harding¹, Michael Jasinski¹, Ron Kwok⁶, Lori Magruder⁷, Dan Lubin⁵, Scott Luthcke¹,
7 James Morison⁸, Ross Nelson¹, Amy Neuenschwander⁷, Stephen Palm¹, Sorin
8 Popescu⁹, CK Shum¹⁰, Bob E. Schutz⁷, Benjamin Smith⁸, Yuekui Yang^{1,11}, Jay Zwally^{1,3}

9

10 ¹NASA Goddard Space Flight Center, Greenbelt, MD

11 ²University of Colorado, Boulder, CO

12 ³University of Maryland, College Park, MD

13 ⁴University at Buffalo, Buffalo, NY

14 ⁵Scripps Institution of Oceanography, La Jolla, CA

15 ⁶Jet Propulsion Laboratory, California Institute of Technology, Pasadena, CA

16 ⁷University of Texas, Austin, TX

17 ⁸University of Washington, Seattle, WA

18 ⁹Texas A&M University, College Station, TX

19 ¹⁰The Ohio State University, Columbus, OH

20 ¹¹Universities Space Research Association, Columbia, MD

21

22 Corresponding author:

23 Thorsten Markus, Thorsten.Markus@nasa.gov, 301-614-5882

24

25 **Abstract**

26

27 The Ice, Cloud, and land Elevation Satellite (ICESat) mission used laser altimetry
28 measurements to determine changes in elevations of glaciers and ice sheets, as well
29 as sea ice thickness distribution. These measurements have provided important
30 information on the response of the cryosphere (Earth's frozen surfaces) to changes
31 in atmosphere and ocean condition. ICESat operated from 2003-2009 and provided
32 repeat altimetry measurements not only to the cryosphere scientific community but
33 also to the ocean, terrestrial and atmospheric scientific communities. The conclusive
34 assessment of significant ongoing rapid changes in the Earth's ice cover, in part
35 supported by ICESat observations, has strengthened the need for sustained, high
36 accuracy, repeat observations similar to what was provided by the ICESat mission.

37 Following recommendations from the National Research Council for an ICESat
38 follow-on mission, the ICESat-2 mission is now under development for planned
39 launch in 2018. The primary scientific aims of the ICESat-2 mission are to continue
40 measurements of sea ice freeboard and ice sheet elevation to determine their
41 changes at scales from outlet glaciers to the entire ice sheet, and from 10s of meters
42 to the entire polar oceans for sea ice freeboard. ICESat carried a single beam
43 profiling laser altimeter that produced ~70 m diameter footprints on the surface of
44 the Earth at ~150 m along-track intervals. In contrast, ICESat-2 will operate with
45 three pairs of beams, each pair separated by about 3 km across-track with a pair
46 spacing of 90 m. Each of the beams will have a nominal 17 m diameter footprint
47 with an along-track sampling interval of 0.7 m. The differences in the ICESat-2

48 measurement concept are a result of overcoming some limitations associated with
49 the approach used in the ICESat mission. The beam pair configuration of ICESat-2
50 allows for the determination of local cross-track slope, a significant factor in
51 measuring elevation change for the outlet glaciers surrounding the Greenland and
52 Antarctica coasts. The multiple beam pairs also provide improved spatial coverage.
53 The dense spatial sampling eliminates along-track measurement gaps, and the small
54 footprint diameter is especially useful for sea surface height measurements in the
55 often narrow leads needed for sea ice freeboard and ice thickness retrievals. The
56 ICESat-2 instrumentation concept uses a low energy 532 nm (green) laser in
57 conjunction with single-photon sensitive detectors to measure range. Combining
58 ICESat-2 data with altimetry data collected since the start of the ICESat mission in
59 2003, such as Operation IceBridge and ESA's CryoSat-2, will yield a 15+ year record
60 of changes in ice sheet elevation and sea ice thickness. ICESat-2 will also provide
61 information of mountain glacier and ice cap elevations changes, land and vegetation
62 heights, inland water elevations, sea surface heights, and cloud layering and optical
63 thickness.

64

65

66

67 **1. Introduction**

68

69 ICESat was the first spaceborne laser altimetry mission for Earth science and was in
70 operation from 2003 – 2009 [Schutz *et al.*, 2005]. Because of laser lifetime issues,
71 ICESat's collection strategy was changed from continual operation to 30 day
72 campaign periods two to three times each year. Despite this campaign mode
73 operation, it was a very successful mission that enabled estimates of the overall
74 mass change of the Greenland and Antarctic ice sheets, as well as the regional
75 changes that illuminate the underlying processes [Pritchard *et al.*, 2009; Zwally *et al.*,
76 2011 and 2015; Sørensen *et al.*, 2011; Sasgen *et al.*, Csatho *et al.*, 2014, Khan *et al.*,
77 2014].

78

79 One of the key findings of ICESat was that some outlet glaciers around the margins
80 of these ice sheets are losing more mass quicker than expected [e.g., Pritchard *et*
81 *al.*, 2009; Zwally *et al.*, 2011]. Investigations using ICESat data resulted in the
82 discovery and subsequent mapping of sub-glacial lakes in Antarctica [Fricker *et al.*,
83 2007; Smith *et al.*, 2009] and the improvement of tide models under ice shelves
84 [Padman *et al.*, 2008; Ray, 2008]. ICESat altimeter data have been used to
85 deconvolve ice and solid earth mass change signals for the Gravity Recovery and
86 Climate Experiment (GRACE) data over Antarctic ice sheets [Gunter *et al.*, 2009;
87 Groh *et al.*, 2012]. Furthermore, ICESat observations provided a comprehensive
88 assessment of ice shelf thinning in Antarctica and subsequent links to dynamic
89 thinning of grounded tributaries (Pritchard *et al.*, 2012).

90
91 Outside of the ice sheets, ICESat data played a critical role in resolving mass changes
92 of mountain glaciers and ice caps (*Moholdt et al.*, 2010, *Gardner et al.*, 2011, *Gardner*
93 *et al.*, 2012, *Moholdt et al.*, 2012) that were determined to have contributed one
94 third of total sea level rise observed over ICESat's period of operation (*Gardner et al.*,
95 2013). Glacier thickness changes from ICESat observations served as a basis to
96 derive the first spatially resolved mass budget over the entire Hindu Kush-
97 Karakoram–Himalaya region (*Kääb et al.*, 2012), the peripheral glaciers, and ice
98 caps of Greenland (*Bolch et al.*, 2013).

99
100 ICESat also demonstrated that it is possible to extract sea ice freeboard, thickness,
101 and volume from laser altimetry [e.g. *Kwok et al.*, 2009; *Farrell et al.*, 2009; *Kurtz and*
102 *Markus, 2012*]. Freeboard is the height of the snow or ice surface above the local sea
103 surface. Sea ice thickness can be derived from freeboard by assuming local
104 hydrostatic balance and with assumptions or estimates of sea ice and water
105 densities as well as snow load on top the ice floes [see, for example, *Kwok et al.*, 2009,
106 *Connor et al.*, 2013, *Farrell et al.*, 2015].

107
108 Time series of inter-annual variation and mission-length trends in sea ice thickness
109 for the entire Arctic and Southern Oceans could be calculated. Recent observations
110 of Arctic sea ice coverage from satellite passive microwave data show that record or
111 near-record lows in ice extents occurred in the years 2005–12. In September 2012,
112 the summer ice extent reached another record minimum of $3.6 \times 10^6 \text{ km}^2$ which was

113 $2.2 \times 10^6 \text{ km}^2$ or 30% less than the record set seven years earlier in September 2005.

114 With this record, seasonal ice now covers more than half of the Arctic Ocean. Results

115 from ICESat showed that over the 5 years (2004-2008) for which we have ICESat

116 data the overall sea ice thickness of the Arctic Ocean multiyear ice decreased by

117 0.6m, and more than 40% of the thick multiyear ice was lost [Kwok *et al.*, 2009].

118 Over decadal time scales, the combined record of submarine and ICESat thickness

119 estimates suggest that winter thickness in the central Arctic has thinned from 3.64

120 m in 1980 to 1.75 m by 2009 [Rothrock *et al.*, 2008; Kwok and Rothrock, 2009].].

121 Extending the ICESat time series with more recent observations from CryoSat-2

122 shows that $\sim 1500 \text{ km}^3$ of winter (February/March) sea-ice volume has been lost

123 from the Arctic Ocean during the last decade between 2003 and 2012 [Laxon *et al.*,

124 2013]. As a result, there is a reversal in both the volumetric and areal contributions

125 of the multiyear and seasonal ice to the total volume and area of the Arctic Ocean ice

126 cover. While thinner, seasonal ice is common in the peripheral seas and ice margins,

127 the Arctic ice cover has clearly shifted to a regime where seasonal ice is now also

128 prevalent in the interior of the Arctic Ocean. With a diminishing multiyear ice cover

129 and thinner ice a significant fraction of the Arctic Ocean is now exposed to the

130 atmosphere during the summer. For the coming decade, thickness estimates are

131 needed for improved subseasonal-to-seasonal forecasts and refined projections of

132 future climate patterns. ICESat also allowed for the first time a rough estimate of sea

133 ice volume of the Antarctic sea ice cover [Kurtz and Markus, 2012].

134

135 Utilizing ICESat sea surface height measurements from leads across the Arctic sea
136 ice pack, together with contemporaneous radar altimetry measurements from
137 Envisat, *Farrell et al.* [2012] described the first mapping of the Arctic Ocean mean
138 dynamic topography using satellite-only data. These sea surface height
139 measurements were also used to derive a high-resolution, satellite-only marine
140 gravity field model of the Arctic [*McAdoo et al.*, 2013].

141

142 ICESat also enabled the estimation of global vegetation heights [e.g. *Harding and*
143 *Carabajal*, 2005; *Lefsky et al.*, 2007], global sea level anomaly and mesoscale
144 variability features [*Urban & Schutz*, 2005], coastal ocean, ocean island and inland
145 hydrology applications [e.g. *Urban et al.*, 2008.], as well as atmospheric
146 characteristics [*Spinhirne et al.*, 2005]. *Lefsky* [2010], *Simard* [2011], and *Los et al.*
147 [2012] generated global canopy height maps using ICESat in combination with other
148 remote sensing data. Since ICESat digitized and recorded the full temporal profile of
149 the received energy, additional research efforts were focused on analyzing specific
150 waveform metrics to determine topographic characteristics and vegetation
151 structure (e.g. *Neuenschwander et al.*, 2008).

152

153 Despite ICESat's success the science community identified some limitations that
154 prohibited the full exploitation of the dataset for scientific applications, particularly
155 for determining change in the cryosphere. Therefore, different needs, requirements,
156 and potential designs were discussed for an ICESat follow-on mission [*Abdalati et al.*,
157 2010]. It was concluded that to understand the governing processes that drive the

158 large-scale changes in glacier and ice sheet elevation and sea ice thickness, changes
159 in elevation should be monitored on a seasonal basis for the lifetime of the mission
160 with improved spatial resolution beyond the observations provided by ICESat. Since
161 the greatest elevation changes are known to occur at the glaciers along the margins
162 of Greenland and Antarctica, there were added complications to the ICESat
163 collection strategy in terms of deconvolving elevation change from surface slope and
164 surface roughness. A single beam laser such as ICESat was not able to separate slope
165 effects from true elevations changes on an orbit-by-orbit basis and thus many years
166 of data were needed to separate these two effects [*Howat et al., 2008; Pritchard et al.,*
167 *2009; Moholdt et al., 2010*]. Improved spatial resolution and the ability to measure
168 the cross-track slope were a critical consideration when developing the ICESat-2
169 mission. The multi-beam instrument design, smaller footprint, and the ability to
170 resolve rougher terrains, would enable more accurate mountain and peripheral
171 glacier mass balance measurements, allowing for improved quantification of land
172 ice contributions to present-day sea level rise.

173

174 Similarly, a smaller footprint size, or rather higher spatial resolution, with increased
175 spatial sampling intervals, will also enhance sea surface height and sea ice freeboard
176 retrievals, and subsequently sea ice thickness calculations. While ICESat's campaign
177 mode allowed the monitoring of inter-annual changes in sea ice thickness, monthly
178 maps of sea ice thickness are needed to better understand freeze and melt processes
179 as well as delineate dynamic versus thermodynamic sea ice thickening.

180

181 It was also determined that ICESat-2 should collect data over the mid- and lower-
182 latitudes for land and ocean areas utilizing an operational off-nadir pointing
183 capability in order to generate an optimized (non-repeat) collection of
184 measurements for canopy heights that will contribute to the generation of a global
185 carbon inventory assessment. Such an inventory is critical for understanding the
186 global carbon budget.

187

188 To this end, the science objectives for ICESat-2 are defined as

189

190 - *Quantify polar ice-sheet contributions to current and recent sea-level change and the*
191 *linkages to climate conditions;*

192

193 - *Quantify regional signatures of ice-sheet changes to assess mechanisms driving those*
194 *changes and improve predictive ice sheet models; this includes quantifying the*
195 *regional evolution of ice sheet change, such as how changes at outlet glacier termini*
196 *propagate inward;*

197

198 - *Estimate sea-ice thickness to examine ice/ocean/atmosphere exchanges of energy,*
199 *mass and moisture;*

200

201 - *Measure vegetation canopy height as a basis for estimating large-scale biomass and*
202 *biomass change.*

203

204 This paper explains how these science objectives translate into science
205 requirements and subsequently into the measurement concept and implementation
206 of the ICESat-2 mission.

207

208 Other areas of Earth science will also benefit from the ICESat-2 mission. The
209 atmospheric community will have access to derived atmospheric and cloud
210 properties while the oceanography community will be given global ocean and wave
211 heights. The hydrological community will be provided global inland water body
212 height and associated properties (*Jasinski et al., 2016*), as well as terrestrial snow
213 thickness and permafrost monitoring.

214

215 **2. Science Requirements**

216

217 Based on the mission objectives established by the ICESat-2 Project together with
218 the ICESat-2 Science Definition Team the following Baseline Science Requirements
219 were developed. These Baseline Science Requirements drive the mission design and
220 the formal requirements flow-down to the spacecraft, instrument, and ground
221 system component level. In addition, Threshold Requirements are defined that
222 represent the minimum requirements that need to be met for the mission to be
223 considered successful in case trade-offs are necessary because of underperforming
224 components.

225

226 *a) ICESat-2 shall produce an ice surface elevation product that enables
227 determination of ice-sheet elevation change rates to an accuracy of better than
228 or equal to 0.4 cm/yr on an annual basis.*

229

230 *For the Threshold Requirement the required accuracy is 2 cm/yr.*

231

232 This high accuracy can be achieved because of the many independent
233 measurements over each of the ice sheets. The value of 0.4 cm/yr for the entire
234 areas of the Greenland and Antarctic ice sheets corresponds to mass changes of 51
235 Gt/yr for Antarctica and 6 Gt/yr for Greenland assuming that all changes occur due
236 to changes in ice thickness with a density of 917 km/m³. For Antarctica, this
237 corresponds to about 85% of the current mass loss (assuming an average of – 60

238 Gt/yr; *Shepherd et al.*, 2012) and to 2.5% of Greenland's mass loss (assuming an
239 average of -240 Gt/yr; *Shepherd et al.*, 2012). While the fraction for Antarctica
240 seems large, Antarctica mass balance estimates range from +100 Gt/yr to about -
241 200 Gt/yr (*Shepherd et al.*, 2012). An accuracy of 51 Gt/yr is about 1/6 of the
242 current mass balance uncertainty. An accuracy of 57 Gt/yr in ice mass balance for
243 the two ice sheets combined corresponds to 0.15 mm in sea level change, which is
244 about ~5% of the current rate (*Hay et al.*, 2015) and ~20% of the error.

245

246 ***b) ICESat-2 shall produce an ice surface elevation product that enables***
247 ***determination of annual surface elevation change rates on outlet glaciers to an***
248 ***accuracy of better than or equal to 0.25 m/yr over areas of 100 km² for year-to-***
249 ***year averages.***

250

251 ***For the Threshold Requirement the required accuracy is 0.5 m/yr.***

252

253 Change detection to 0.25 m/yr will enable the detection of dynamically-significant
254 changes in outlet glaciers. For most Greenland outlet glaciers, the rate of surface
255 elevation change is on the order of a few meters to tens of meters per year, with
256 progressively smaller changes farther upstream [*Pritchard et al.*, 2009; *Thomas et al.*,
257 2009]. Typical Greenland outlet glaciers are on the order of 2-5 km wide and 20-50
258 km long, so 100 km² is a typical area scale for the fast-changing parts of the ice sheet.
259 Measuring elevation changes to 0.25 m/yr will enable the determination of the
260 magnitude of outlet glacier changes, and will allow the monitoring of the extent to

261 which changes in the outlets are driving smaller changes, over larger areas, in the
262 inland ice sheet. Understanding the inland extent of elevation changes driven by the
263 outlets is critical for understanding the potential future contributions of Greenland
264 and Antarctica to sea level rise [Price *et al.*, 2011].

265

266 In Antarctica, where elevation change rates are smaller, greater accuracy is required.
267 However outlet glaciers are generally larger in Antarctica, and the expectation is
268 that the characteristics of the measurement error (e.g., correlation lengths) will be
269 such that measurements will have sufficient accuracy for most large Antarctic outlet
270 glaciers.

271

272 **c) ICESat-2 shall produce an ice surface elevation product that enables**
273 **determination of surface elevation change rates for dynamic ice features that**
274 **are intersected by its set of repeated ground-tracks to an accuracy of better**
275 **than or equal to 0.4 m/yr along 1-km track segments.**

276

277 **For the Threshold Requirement the required accuracy is 0.8 m/yr.**

278

279 One of the biggest unexpected discoveries of ICESat was the number, size, and
280 dynamics of subglacial lakes located under the Antarctic ice sheet. [Smith *et al.*, 2009,
281 Fricker *et al.*, 2007]. Analysis of repeated ICESat tracks showed unexpected large
282 elevation changes over many areas of the assumed stable inland Antarctic ice sheet.
283 Similarly, ICESat repeat-track data have also been useful in measuring grounding-

284 line positions based on short-scale pass-to-pass surface changes. [Fricker *et al.*, 2009,
285 Brunt *et al.*, 2010, Brunt *et al.*, 2011]. The exact repeat-track orbit of ICESat enabled
286 these studies of small-scale elevation changes and similar repeat tracks for ICESat-2
287 will enable the continuation of both of these types of studies, and, over the course of
288 the mission, will allow estimates of grounding-line change for Antarctic ice shelves
289 and Greenland outlet glaciers.

290

291 ***d) ICESat-2 shall produce an ice surface elevation product that enables***
292 ***resolution of winter (accumulation) and summer (ablation) ice-sheet elevation***
293 ***change to 10 cm at 25-km x 25-km spatial scales.***

294

295 ***For the Threshold Requirement the required accuracy is 5 cm but is limited to***
296 ***areas with a slope of less than 1 degree (essentially excluding outlet glaciers).***

297

298 This accuracy represents approximately 10% of the seasonal amplitude of ice
299 surface elevation change for coastal Greenland. Measuring seasonal elevation
300 changes offers multiple benefits to cryospheric studies: It allows calibration of
301 atmospheric models estimating accumulation and ablation from the ice sheets
302 [Ligtenberg *et al.*, 2012] and validation of firn densification models [Munneke *et al.*,
303 2015]. It also provides mass change time series comparable in accuracy and
304 temporal resolution to gravimetric estimates of ice-sheet change (i.e. from GRACE),
305 and it will allow the subtraction of the surface-mass-balance-driven elevation

306 change from outlet-glacier elevation changes, isolating the dynamic signal [Csatho et
307 al., 2014].

308

309 **e) ICESat-2 shall provide monthly surface elevation products to enable, when**
310 **sea surface height references (leads) are available and under clear sky**
311 **conditions, the determination of sea-ice freeboard to an uncertainty of less than**
312 **or equal to 3 cm along 25-km segments for the Arctic and Southern Oceans; the**
313 **track spacing should be less than or equal to 35 km at 70 degrees latitude on a**
314 **monthly basis.**

315

316 **The Threshold Requirement retains the 3 cm freeboard uncertainty but relaxes**
317 **the length scale to 50 km.**

318

319 Deriving sea ice freeboard and subsequently sea ice thickness and changes in
320 thickness requires the ability to discriminate the sea surface height from
321 surrounding sea ice height for freeboard determination. Since only a small fraction
322 (roughly 1/10) of the floating sea ice is above the water level, small errors in
323 freeboard retrieval can result in large errors in the scaling of freeboard to estimates
324 of sea ice thickness. The required 0.03 m height measurement precision
325 corresponds to an accuracy of ~0.3 m in thickness or an overall uncertainty of less
326 than 25% of the current annual ice-volume production of the Arctic Ocean.
327 Measurement at this level will enable accurate determination of the spatial ranges of
328 mean ice thickness of 2 to 3 meters across the Arctic and Southern Oceans.

329 Furthermore, monthly data sampling of the ice-covered Arctic and Southern Oceans
330 is required to resolve the seasonal cycles in ice growth and decay. Monthly averages
331 are the longest temporal scale that can be used to create coherent sea ice thickness
332 maps without significant interference of the seasonal cycle. ICESat-2's dense along-
333 track sampling, and multi-beam configuration, will also provide detailed knowledge
334 of sea ice surface characteristics and morphology.

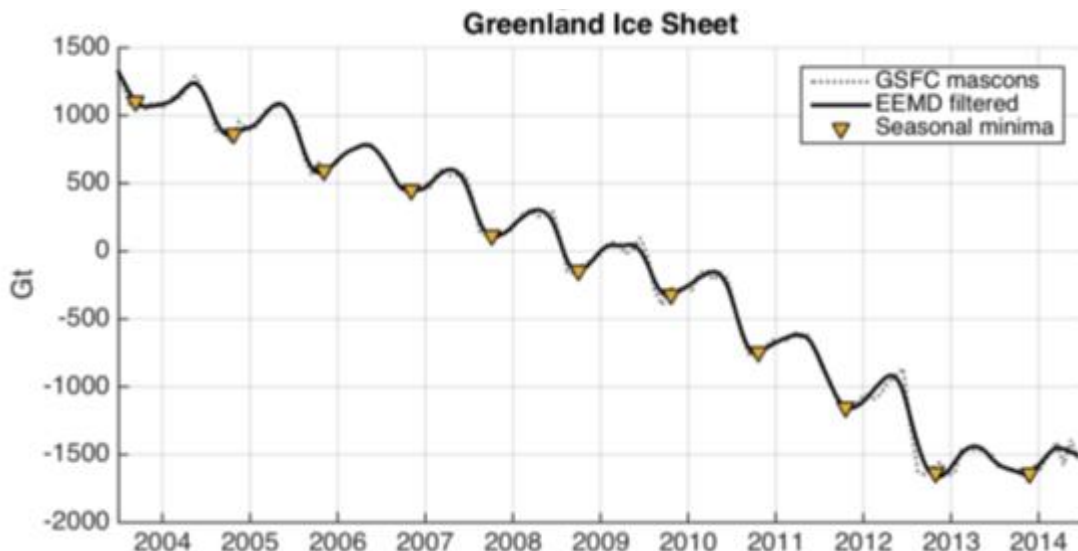
335

336 **f) ICESat-2 shall make measurements that span a minimum of three years.**

337

338 **The Threshold Requirement retains the three year operation requirement but**
339 **allows the mission to only take science data for 182 day per year providing at**
340 **least seasonal sampling.**

341



342

343 *Figure 1: Greenland ice sheet cumulative mass change time series from NASA GSFC*
344 *mascon solution (update to Luthcke et al., 2013). Mascon solution shown as dashed*

345 *line with Ensemble Empirical Mode Decomposition (EEMD) filtered mascon solution*
346 *time series as solid line with seasonal minima determined from EEMD analysis (Loomis*
347 *and Luthcke, 2014)). Significant inter-annual variations are observed including the*
348 *extreme summer mass loss in 2012 followed by the recent pause in mass loss.*

349

350 The mass evolution of the ice sheets exhibits significant seasonal and inter-annual
351 variations as observed by satellite gravimetry (Luthcke *et al.*, 2013). Figure 1
352 presents the mass evolution of the Greenland ice sheet from a recent NASA GSFC
353 GRACE mascon solution (update to Luthcke *et al.*, 2013). The time series exhibits
354 significant inter-annual variation including the extreme 2012 summer mass loss
355 followed by a pause in mass loss. A minimum of 3 years of ICESat-2 observations
356 are necessary to fully observe the seasonal and inter-annual variations in order to
357 compute the mass balance from ICESat-2, the decadal ICESat and ICESat-2 inter-
358 mission mass balance, and to facilitate comparison and combination with GRACE
359 and GRACE-Follow-On data for a multi-decadal mapping of ice sheet change.

360

361 The Threshold Requirement allows, if necessary, to operate ICESat-2 in a campaign
362 mode similar to ICESat in order to increase mission lifetime, but still capture the
363 extremes and inter-annual variations of the seasonal cycle.

364

365 ***g) ICESat-2 shall produce an ice surface elevation product that, in conjunction***
366 ***with ICESat, enables determination of elevation changes on a decadal time scale.***

367

368 ***This requirement is unchanged for the Threshold Requirements.***

369

370 The detailed Greenland Ice Sheet laser altimetry record (1993-2012) using both
371 airborne and satellite data shows large spatial and temporal variations of dynamic
372 mass loss and widespread intermittent thinning with rapid thinning periods lasting
373 from a few years to more than 15 years [Csatho et al., 2014]. This complexity of ice
374 sheet response to climate forcing points to the need for decadal or longer
375 monitoring of the ice sheets at high spatial resolution. Careful monitoring of
376 measurement biases, trends, and errors is needed for the establishment of a long
377 time series.

378

379 ***h) ICESat-2 shall produce elevation measurements, that enable independent***
380 ***determination of global vegetation height, with a ground track spacing of less***
381 ***than 2 km over a 2-year period.***

382

383 ***This requirement is deleted in the Threshold Requirements.***

384

385 Forests play a significant role in the terrestrial carbon cycle as carbon pools. Events,
386 such as management activities [Krankina et al. 2012] and disturbances can release
387 carbon stored in forest above ground biomass into the atmosphere as carbon
388 dioxide, a greenhouse gas that contributes to climate change [Ahmed et al. 2013].
389 While carbon stocks in nations with continuous national forest inventories (NFIs)
390 are known, complications with NFI carbon stock estimates exist, including: (1)

391 ground-based inventory measurements are time consuming, expensive, and difficult
392 to collect at large-scales [Houghton, 2005; Ahmed *et al.* 2013]; (2) asynchronously
393 collected data; (3) extended time between repeat measurements [Houghton, 2005];
394 and (4) the lack of information on the spatial distribution of forest above ground
395 biomass, required for monitoring sources and sinks of carbon (Houghton, 2005).

396

397 Based on the global carbon budget for 2015 [Le Quere *et al.*, 2015], the largest
398 remaining uncertainties about the Earth's carbon budget are in its terrestrial
399 components, the global residual terrestrial carbon sink, estimated at $3.0 +/- 0.8 \text{ GtC}$
400 /year for the last decade (2005-2014). Similarly, carbon emissions from land-use
401 changes, including deforestation, afforestation, logging, forest degradation and
402 shifting cultivation are estimated at $0.9 + - 0.5 \text{ GtC} / \text{year}$. By providing information on
403 vegetation canopy height globally with a higher spatial resolution than previously
404 afforded by other spaceborne sensors, the ICESat-2 mission can contribute
405 significantly to reducing uncertainties associated with forest vegetation carbon.

406

407 It is anticipated that the data products for vegetation will be complementary to
408 ongoing biomass and vegetation mapping efforts. Synergistic use of ICESat-2 data
409 with other space-based mapping systems (e.g. the Global Ecosystem Dynamics
410 Investigation Lidar (GEDI); <https://science.nasa.gov/missions/gedi/>) or imaging
411 sensors, such as optical or radar (e.g. the NASA-ISRO SAR Mission (NISAR);
412 <http://nisar.jpl.nasa.gov>), is one solution for extended use of ICESat-2 data.

413

414 ***i) The ICESat-2 Project shall conduct a calibration and validation program to***
415 ***verify delivered data meet the requirements a, b, c, d, e, g and h.***

416

417 ***This requirement is unchanged for the Threshold Requirements.***

418

419 Calibration and validation of the ICESat-2 products is a critical component of the
420 mission. Rigorous effort is required during pre-launch studies as the
421 instrumentation is characterized and relevant models are developed to support an
422 accurate understanding of the operational aspects of the instrument as
423 environmental and mechanical parameters vary. Additionally, a comprehensive
424 calibration and validation plan will be initiated once ICESat-2 is on orbit in order to
425 establish an accurate understanding of all of the ICESat-2 data products in terms of
426 uncertainties and potential biases. This effort will establish confidence in the
427 scientific data and verify that the requirements of the mission have been achieved.

428 This requirement is obvious because without calibration and validation and without
429 rigorous uncertainty and error assessment any geophysical products would remain
430 questionable.

431

432 **3. Measurement and mission concept**

433

434 The baseline requirements above drive the top-level mission design, its
435 implementation, and operations plan. The ICESat-2 mission carries a single
436 instrument, the Advanced Topographic Laser Altimeter System (ATLAS). This
437 section is divided into descriptions of the required sampling geometry, elevation
438 precision, bias monitoring, geophysical corrections, and coverage. All are critical
439 aspects considered when developing ICESat-2 and ATLAS technical capabilities.

440

441 The measurement concept of the ICESat-2 instrument is quite different from an
442 analog laser altimeter like onboard ICESat. The ICESat-2 micropulse laser will
443 produce much less energy per pulse but with a 10kHz repetition rate. This increased
444 repetition rate will result in a 0.7 m separation for each laser pulse on the surface.
445 This is ideal for rough and heterogeneous terrain such as glaciers or sea surface
446 heights where the minimal gaps in along-track measurements will provide a higher
447 fidelity of the topography. The inherent detection requirement associated with the
448 lower power of the micropulse laser are detector sensitivities on the single photon
449 level. This requirement is achieved through the use of photomultiplier tubes (PMTs)
450 as detectors where single photons reflected from the surface will trigger a detection
451 within the ICESat-2 receiver. Each individual photon will be time tagged and
452 geolocated. This scenario is much different than the full-waveform data collected by
453 ICESat for each laser footprint.

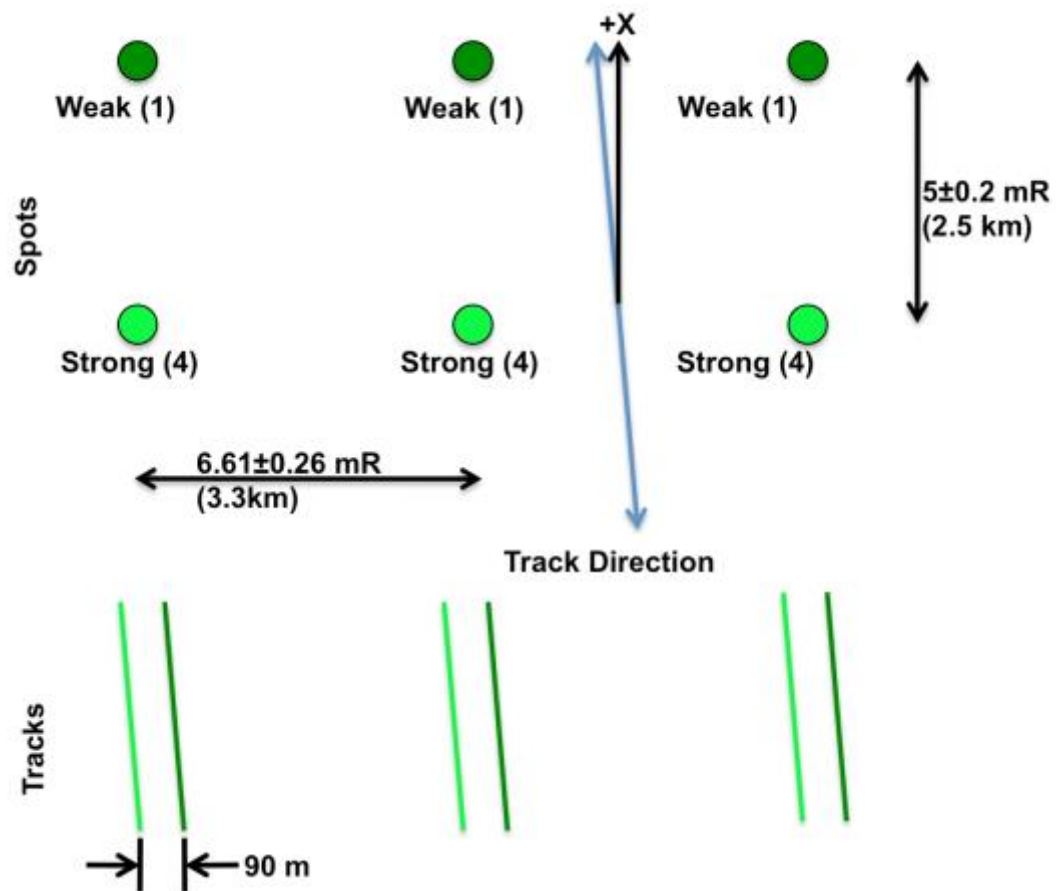
454

455 3.1. Sampling geometry

456

457 ICESat-2 will have a total of 6 beams organized in a 2x3 array. By slightly yawing the
458 spacecraft during flight this will create three pairs of beams on the ground with each
459 pair being separated by 3.3 km and a pair width of 90 m (see Figure 2). The pair
460 width is adjustable on orbit by changing the yaw angle.

461



462

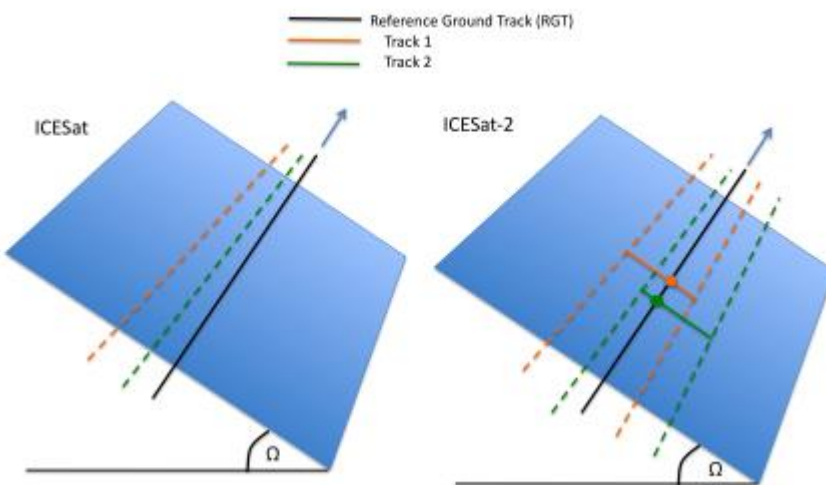
463 *Figure 2: ICESat-2's sampling geometry. The beam pattern is a 3 x 2 array that, by*
464 *slightly yawing the spacecraft, creates three pairs of beams on the ground. The*

465 planned separation for each pair is 90 m but this can be changed on orbit by changing
466 the yaw angle.

467

468 To achieve high spatial resolution and discriminate elevation change from cross-
469 track surface slope, closely separated pairs of beam are required. This is a critical
470 capability needed to meet the science requirements associated with the ice sheets in
471 particular. Figure 3 depicts the differences in the collection strategy of ICESat and
472 ICESat-2 where the multi-beam configuration supports annual and seasonal
473 elevation change determination independent of cross-track surface slope.

474



475

476 Figure 3: Comparison of elevation change retrievals from ICESat and ICESat-2. With
477 an unknown slope Ω and near coincident tracks it is impossible to calculate elevation
478 change from two single-beam tracks (ICESat; left). ICESat-2 (right) has pairs of beams
479 that straddle the reference ground track so that its elevation can be extracted through
480 interpolation of the elevations measured by the two beams.

481

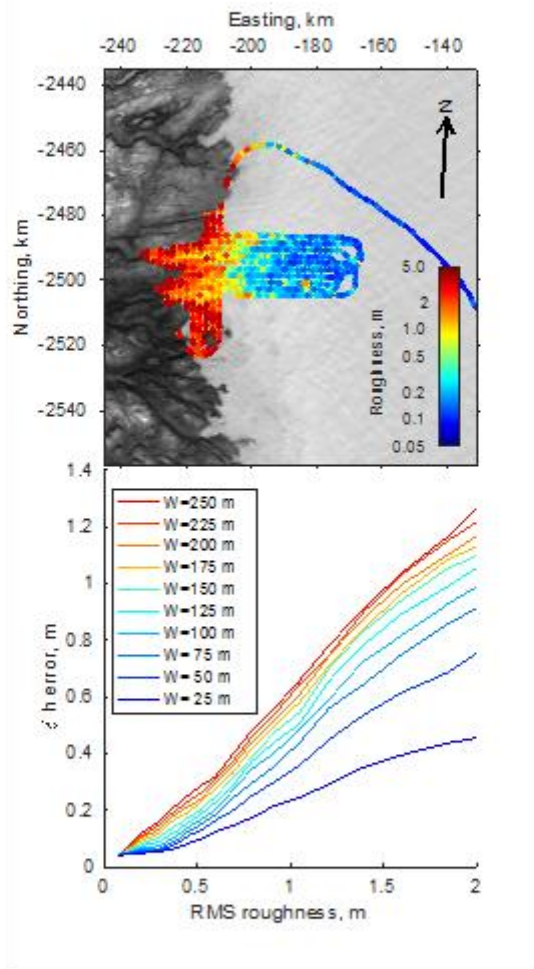
482 The location of the laser spot will not perfectly follow the reference ground tracks
483 (RGT) for repeated measurements due to limitations in pointing control. The actual
484 laser spots may be a slightly offset (the orange and green lines in Fig. 3) from the
485 RGT (black lines in Fig. 3). To meet the science objectives and ice sheet science
486 requirements, ICESat-2 will utilize pairs of beams (Fig. 3, right side). The concept is
487 that each time the satellite passes over the RGT one beam is to the left and one to
488 the right of the RGT. This makes it possible to calculate the local cross-track slope
489 and interpolate the elevation to the RGT. Because cross-track surface slope is not
490 known a-priori it is ambiguous whether the elevation derived from subsequent
491 passes is real change or whether the measured elevation differences are a result of
492 track location differences over a sloped surface. For ICESat several years of data
493 were required to extract the surface slope (assuming the slope did not change over
494 that time period) before the elevation change could be determined [e.g. *Howat et al.*,
495 2008; *Pritchard et al.*, 2009; *Smith et al.*, 2009; *Moholdt et al.*, 2010]. Multiple beam
496 pairs will mitigate the uncertainties associated with the assumptions of surface
497 slope characteristics ensued from ICESat single beam collection configuration.

498

499 A pair-spacing requirement of 90 m is based on a sampling analysis of airborne
500 laser-altimetry data collected with the Airborne Topographic Mapper (ATM) over
501 Russell Glacier, in Southwest Greenland, which spans a wide range of surface
502 roughnesses (Figure 4, top). In this analysis, the collection of point elevation
503 measurements was sampled using different potential beam spacings and random
504 repeat-track geometries, and the RMS error calculated in the resulting surface-

505 change measurements. Figure 4, bottom, shows the elevation-difference accuracy as
506 a function of surface roughness for different beam spacings. For all roughness values,
507 the error increases with the pair spacing, but for the small (<0.5 m) roughnesses
508 typical of the interior of the ice sheet, the ICESat-2 error is small for spacings less
509 than 100 m, increasing sharply for larger spacings. This reflects the lack of
510 significant surface topography at scales smaller than about 100-200 m over
511 uncrevassed ice, which lets repeat track sampling at scales finer than 100 m correct
512 for the shape of the surface topography, while at larger spacings, the fine-scale
513 topography is undersampled and leads to an elevation-change error. To interpolate
514 to the RGT, ICESat-2 needs to control the beam position to less than half the pair
515 separation. Thus a pointing control ≤ 45 m is required.

516



517

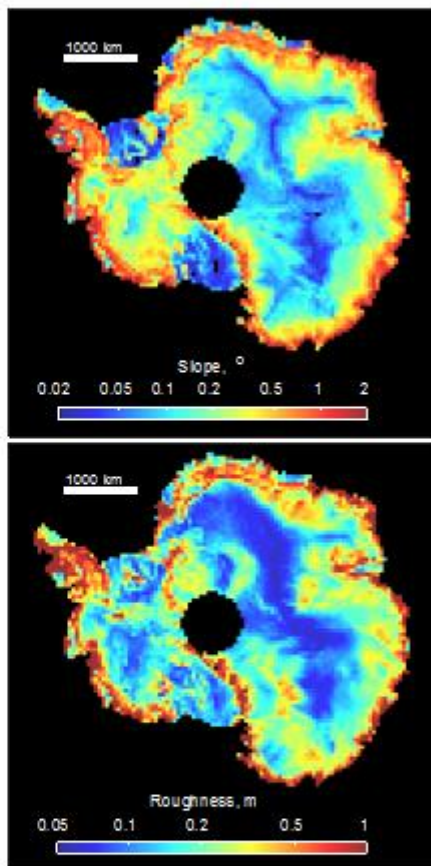
518 *Figure 4: Top: surface roughness, calculated as the RMS difference between elevation
 519 measurements and 200-meter linear segments, measured over lower Russell Glacier,
 520 Southwest Greenland. The scale is about 100 km horizontal and vertical. Northing and*

521 *Easting give coordinates in a polar stereographic projection with a true-scale at 70N*
522 *and a central meridian of -45E. Bottom: Height-recovery errors as a function of beam*
523 *spacing (W) and surface roughness for simulated ICESat-2 data. Roughness values less*
524 *than 0.5 m are typical of inland ice while larger values reflect surface crevassing.*

525

526 One component of the elevation error over areas with surface slope is directly
527 related to geolocation knowledge derived in post-processing multiplied by the
528 tangent of the slope. The requirement for pointing knowledge after post-processing
529 is 6.5 m, which translates into an elevation error of about 0.5 m over slopes with 5
530 degrees, a typical slope of the glaciers along the coasts of the Greenland and
531 Antarctic ice sheets. For most of the ice sheets the slope is much smaller (Figure 5).
532 Figure 5 shows the surface slope magnitude and roughness calculated from ICESat
533 elevation data, masked using information from a visible-imagery mosaic of
534 Antarctica [Haran *et al.*, 2005] to include only ice-sheet surfaces. These data cover
535 the ice sheet to a latitude of 86 degrees, and accurately resolve variations in surface
536 slope at horizontal scales as small as 170 m. Slopes are small ($< 0.5^\circ$) except near
537 coasts and where glaciers flow through mountains. Surface roughness is also small
538 (< 0.25 m) except in coastal areas, in crevassed shear margins, and in a few parts of
539 the ice-sheet interior where wind erosion produces meter-scale surface features.

540



541

542 *Figure 5: Top: Ice sheet surface slope magnitude for the entire continent of Antarctica,*
543 *calculated as the 68th percentile of surface slopes for 50x50 km squares on the ice-*
544 *sheet surface. Data are in a polar stereographic projection with a true-scale at 70S.*

545 *The south pole is in the center of the figure with 0E straight up. Bottom, ice sheet*
546 *roughness calculated as the 68th percentile of the absolute difference between each*
547 *measured elevation and the average of its two nearest along-track neighbors, for the*
548 *same grid used for the slope map.*

549

550 ICESat-2's orbit will have an inclination of 92 degrees enabling measurements up to
551 88 degrees north and south, with a 91-day exact repeat cycle. This will ensure
552 seasonal repeat tracks that are needed for the seasonal ice sheet requirement
553 (requirement d). Because, as stated in Requirement e), Arctic- and Southern Ocean-
554 wide sea ice freeboard maps shall be generated on a monthly basis an orbit was
555 chosen with a near-monthly sub-cycle resulting in an even distribution of tracks
556 every month. Since ICESat took measurements in 30-day campaign modes, the
557 actual increase in coverage compared to ICESat is nine times over a 91 period.

558

559 3. 2. Elevation precision

560

561 Individual, timed and geolocated, photons do not in themselves provide direct
562 information of the elevation of the surface because a priori the source of any given
563 photon is unknown. It may have originated from reflection of a laser pulse off a
564 cloud or sunlight of the same wavelength may have scattered back into the telescope.
565 Photons from several shots need to be accumulated and statistically analyzed.
566 Statistically the density of photons reflected from the surface is much greater than
567 the more evenly distributed photons from the atmospheric column so that the

568 elevation of the earth surface can be determined using statistical characteristics and
569 noise filtering. The actual elevation precision depends on the signal-to-noise ratio,
570 on the length or distance over which laser shots are accumulated, and the precision
571 with which each photon can be timed. Model calculations were used to predict
572 ICESat-2's radiometric performance over various surfaces and the results guided
573 requirements flowdown and instrument design. Not all beams have the same energy
574 to keep the required laser energy low and because cross-track slope retrieval is only
575 needed for the highly reflective ice sheets where the number of signal photons is
576 high. Therefore, each beam pair consists of a strong and a weak beam. The strong
577 beam has four times the energy of the weak beam and consequently four times the
578 number of returned laser photons per shot.

579

580

581 Table 1 shows the predicted number of return photons received per shot for
582 different surface types and also the standard deviations of range for 100 shot
583 accumulations, which is equal to 70 m along track. Return strength in
584 photoelectrons per shot was calculated using the transmitted energy, the
585 instrument optical throughput and detector efficiency, and atmospheric and surface
586 reflectance parameters that define each design case. The temporal distribution of
587 return photoelectrons was modeled using a transmitted pulse profile and receiver
588 impulse response, and surface impulse responses derived from the surface
589 parameters such as slope, roughness and type (ice or water) that define each design
590 case. The number of detection events per shot was calculated using the number and

591 distribution of photoelectrons and a model of the PMT's deadtime behavior. The
592 range in the number of expected return photons and standard deviations for each
593 surface type is a function of the environmental conditions such as surface roughness
594 and reflectance. For high reflectivity targets, such as ice sheets, the weak beams
595 returns a sufficient number of laser photons to enable elevation measurements.

596

597 *Table 1: ATLAS expected performance in range using the current best estimates for*
598 *winter and summer conditions.*

Target type	Lambertian surface reflectance (532 nm)	N signal photons per shot (weak beam)	N signal photons per shot (strong beam)	100-shot std dev (weak beam) [cm]	100-shot std dev (strong beam) [cm]
Ice sheet (interior)	0.9 – 0.98	0.4 – 3.0	1.6 – 12.0	4 – 9	2 - 4
Ice sheet (glaciers)	0.6 – 0.9	0.6 – 1.0	0.6 – 3.9	12 – 29	6 - 14
Sea ice	0.8 – 0.9	0.6 – 2.1	2.3 – 8.5	5 – 8	3 - 4
Leads	0.1 – 0.2 (much higher when specular)	0.05 – 0.2	0.2 – 1.0	2 – 5	2 - 5

599

600 To enable the development of retrieval algorithms, an ICESat-2 airborne simulator,
601 the Multiple Beam Experimental Lidar (MABEL) [McGill *et al.*, 2013], was flown over
602 sea ice [Kwok *et al.* 2014; Farrell *et al.*, 2015], ice sheets [Brunt *et al.*, 2014; Brunt *et*
603 *al.*, 2016], vegetated areas [Herzfeld *et al.*, 2014; Gwenzi and Lefsky, 2014, Glenn *et al.*,
604 2016], cities, oceans, and lakes [Jasinski *et al.*, 2016] during different seasons.

605 MABEL's pulse repetition rate is variable (5 to 25 kHz) and was 5 kHz for the data
606 presented here. At this nominal altitude and repetition rate, and at an aircraft speed
607 of \sim 200 m s $^{-1}$, MABEL samples a \sim 2 m footprint every \sim 0.04 m along-track. More
608 specifications on MABEL are given in Appendix A. The spacing between the
609 individual beams was configured to allow simulation of the planned beam geometry
610 of ATLAS. Owing to non-uniform optical paths (fiber lengths) through the
611 instrument, the transmit-pulse energies are generally not equal. Consequently, the
612 number of signal photons per shot was also not equal. They furthermore differed
613 between the different campaigns.

614

615

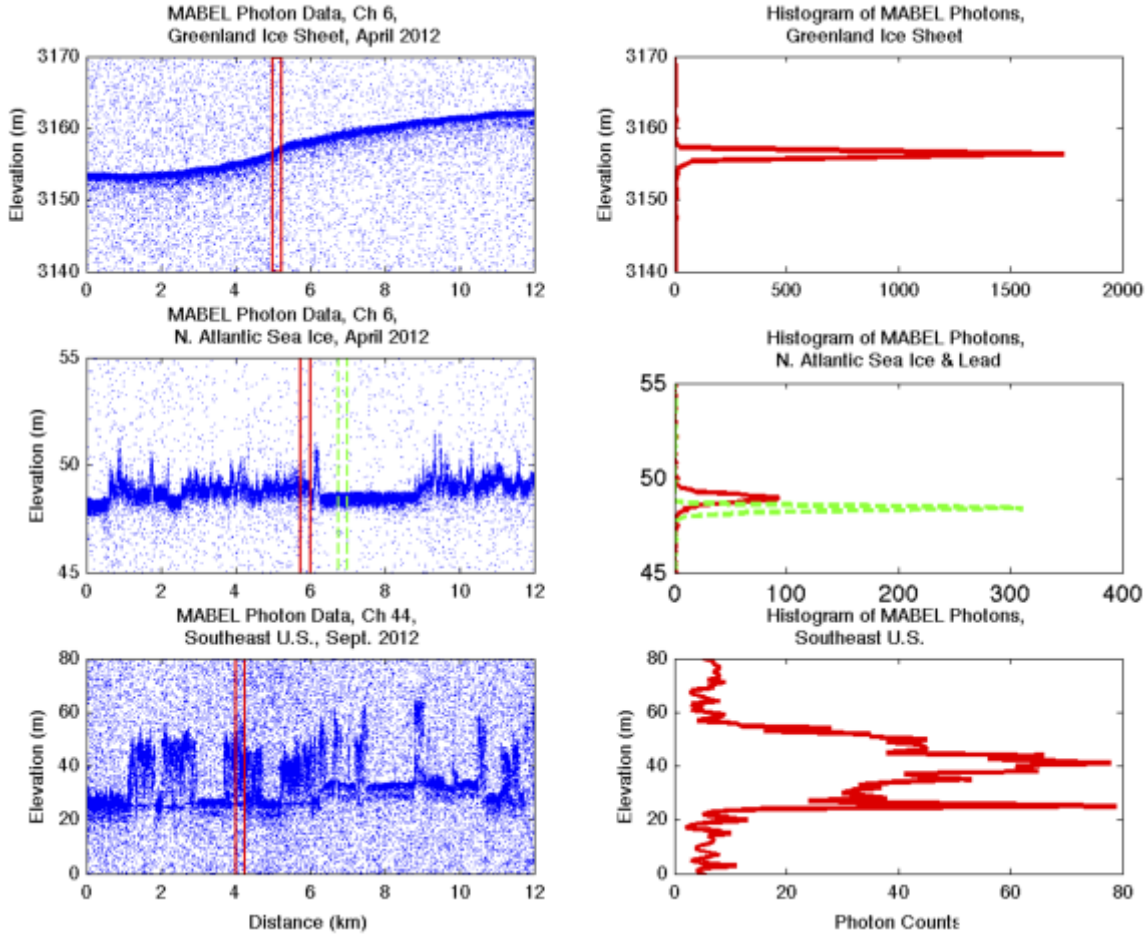
616

617 Descriptions of the campaigns as well as the data are available via <http://icesat->
618 2.gsfc.nasa.gov/data. The data collections were planned to provide the critical
619 sample data needed in the development of the ICESat-2 algorithms by varying
620 surface type and season of acquisition. The altitude of many of these flights was
621 about 20 km (65,000 ft) above sea level so that 95% of the atmospheric contribution
622 was between the instrument and the Earth's surface. This facilitates the
623 development of algorithms for atmospheric properties and also provides realistic
624 atmospheric photon distributions that may impact the ground finding algorithms.

625 Figure 6 shows some examples from these flights for three surface types.

626

627



628

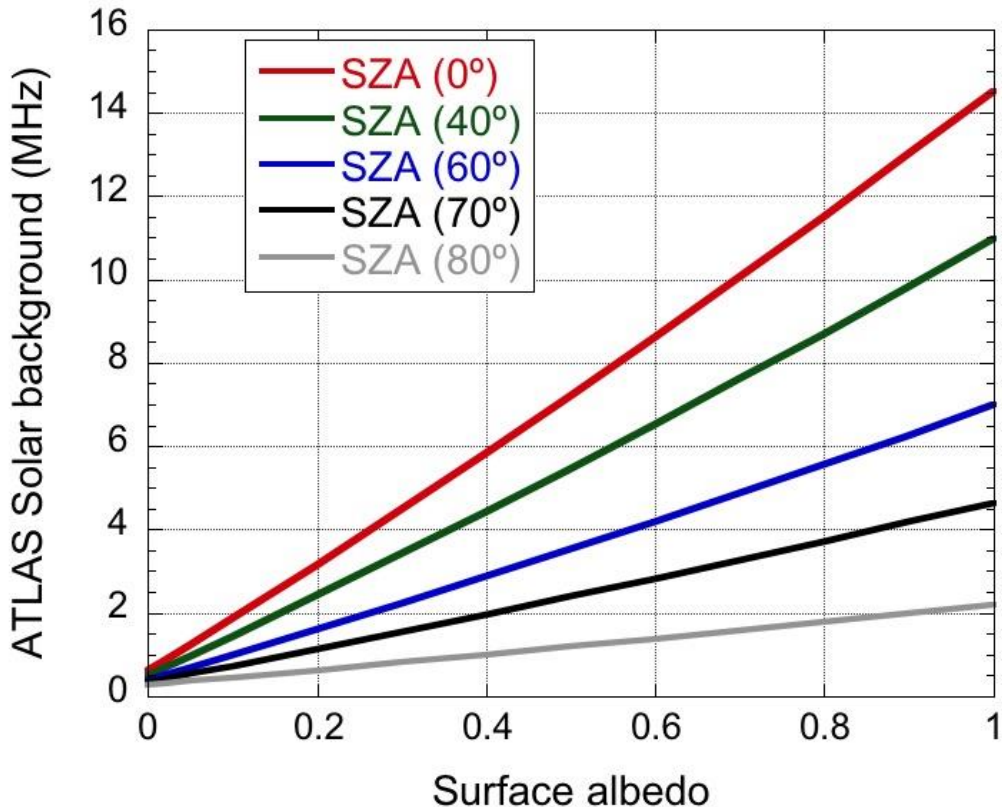
629 *Figure 6: Typical ICESat-2-like data from MABEL over the Greenland ice sheet (top),*
 630 *sea ice (middle), and vegetated land surface (bottom). The histograms on the right*
 631 *show photon distributions for the areas between the two red and green vertical lines in*
 632 *the photon clouds. The distance between the lines is 200 m for these examples. In the*
 633 *actual algorithms that are currently being developed for operational processing this*
 634 *distance will be optimized and may vary as a function of signal-to-noise ratio, surface*
 635 *roughness, and number of signal photons.*

636

637 The data show the time-tagged photon elevations as a function of distance along-
 638 track (Figure 6, left panel). While there appear a significant number of solar photons

639 in all three examples, the number of photons reflected from the surface is much
640 greater and densely clustered compared to the more evenly distributed photons
641 from either the atmosphere or solar background so that the elevation of the earth
642 surface and also its properties can be extracted. The number of solar photons is
643 primarily a function of the surface reflectivity and the solar angle. As shown in
644 Figure 7, for a Lambertian surface, the highest clear sky solar background rate is
645 about 14.5 MHz (for overhead sun), but since most of the high albedo areas are in
646 the polar regions, where the solar zenith angles are generally large, high
647 background rates of solar photons are about 10 MHz, which translates to two solar
648 photon every ~60 m vertically. At night these photons will be minimal. The
649 detectors themselves also are subject to some noise but measurements have shown
650 that the detector dark count rate is 1000 Hz and thus negligible. The quantitative
651 estimate of surface elevation and canopy heights is done by the generation of
652 histograms (Figure 6, right panel) of photon densities and statistical analyses. This
653 is an active area of research as algorithms are being developed primarily using
654 MABEL data [Kwok *et al.* 2014; Farrell *et al.*, 2015; Brunt *et al.*, 2014; Brunt *et al.*,
655 2016; Herzfeld *et al.*, 2014; Gwenzi and Lefsky, 2014, Glenn *et al.*, 2016; Jasinski *et al.*,
656 2016].

657



658

659

660 *Fig. 7: ATLAS clear sky solar photon rate as a function of surface albedo for different*
 661 *Solar Zenith Angles (SZA). Surface is assumed Lambertian. Simulations done with the*
 662 *Discrete Ordinates Radiative Transfer model (DISORT) [Stamnes et al. 1988]. ATLAS*
 663 *parameters used in the calculations include: telescope diameter (0.8 m), field of view*
 664 *(85μrad), detector quantum efficiency (0.15), total receiver transmission (0.504) and*
 665 *filter width (0.038nm).*

666

667 The top row of Fig.6 shows an example of the interior Greenland ice sheet. For these
 668 relatively flat areas, the 200 m histogram has a very clear peak above the noise,
 669 enabling the identification of surface elevation. Figure 6 also indicates that for
 670 smooth high-reflectivity area, histograms over much shorter distances will be

671 sufficient to extract surface elevation with high confidence, increasing the along-
672 track spatial resolution of elevation retrievals. Because each received photon is
673 timed and geolocated, the length over which photons are accumulated for the
674 calculation of surface elevation is flexible and can be optimized in algorithms
675 depending on accuracy and precision requirements.

676

677 For sea ice (Fig.6, middle plots), there is an elevation difference between the flat
678 leads and the rougher and higher sea ice. To estimate the freeboard, elevations of
679 both the sea ice and the open water need to be calculated. The red vertical lines for
680 sea ice and green vertical lines for the open water indicate example areas. The
681 corresponding histograms have peaks at different elevations, which directly
682 correspond to the sea ice freeboard. *Kwok et al.* [2014] and *Farrell et al.* [2015]
683 provide a detailed discussion of the identification of leads using MABEL data for the
684 retrieval of sea surface heights and the derivation of freeboard and thickness.

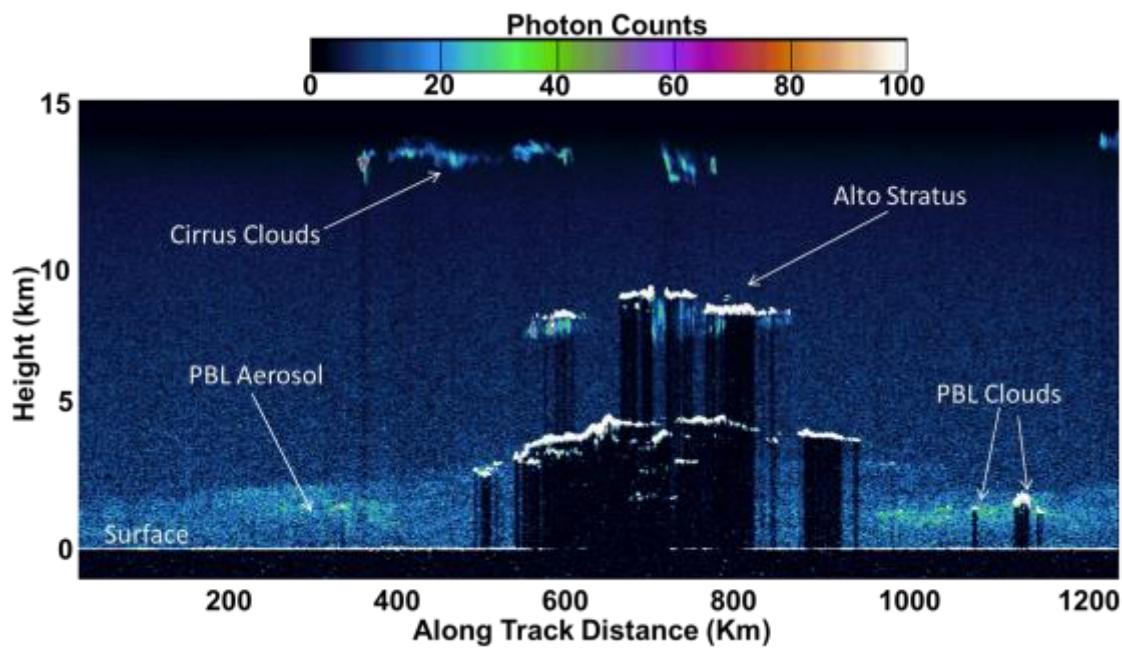
685

686 Figure 6 (bottom) shows an example of MABEL returns over vegetation. The
687 histogram of photons between the red lines shows two distinct peaks. The upper,
688 broader, peak is from photons reflected off the tree crowns whereas the lower,
689 sharper peak is from the ground surface below the trees. Analysis of histograms or
690 photon densities will allow the retrieval of tree heights and potentially also yield
691 information of tree structure or type [*Glenn et al.*, 2016]. The strength of the ground
692 surface signal is a function of canopy density.

693

694 In addition to surface products, ICESat-2 will also collect data for the entire lower
695 atmosphere. While every photon around the surface will be timed and geolocated to
696 preserve full resolution and highest elevation accuracy, data over the atmospheric
697 column are accumulated 30 m vertically and 280 m along-track onboard the
698 spacecraft to reduce data volume. Figure 8 shows a plot of photon densities
699 collected by the MABEL instrument. Areas of higher densities can be attributed to
700 different types of clouds. The flat line of high photon densities at the bottom of
701 Figure 6 are from surface returns. When the cloud optical depth becomes too high
702 the surface signal is lost.

703



704

705 *Figure 8: Photon densities for a 15 km range in altitude and horizontal distance of*
706 *about 100 km; the brighter the color the higher the photon density. In addition to the*
707 *surface different types of clouds (PBL stands for "planetary boundary layer") can be*

708 identified. Data were taken with the MABEL instrument on September 21, 2013 over
709 the southern portion of the Chesapeake Bay.

710

711 3.3 Bias monitoring

712

713 Most ICESat-2 requirements are expressed in elevation change. It is therefore
714 imperative to monitor changes in the instrument bias that may be expressed as
715 range or elevation change. Several measures are taken to ensure that instrument
716 changes are monitored and accounted for in post-processing. The mission has a
717 requirement to monitor changes in elevation bias to 0.2 cm per year over the full life
718 of the mission and to provide long-term trend analyses of observatory performance.

719 Pre-launch, the instrument team will characterize the change in range bias as a
720 function of telemetered temperatures. On orbit, the instrument will monitor and
721 calibrate changes in range bias using Transmit Echo Calibration. The Transmitter
722 Echo is a small sample of the transmitted pulse, carried directly to the receiver by
723 fiber optics. Monitoring its measured time of flight will indicate any changes in the
724 receiver's timing bias. This will be done for two beams and the results can be
725 compared to the pre-launch data. In post-processing data analysis, range bias
726 changes for the other four beams will be examined by comparing short-period (< 24
727 hrs) crossovers (in 10-day groups) of the calibrated with the un-calibrated beams.

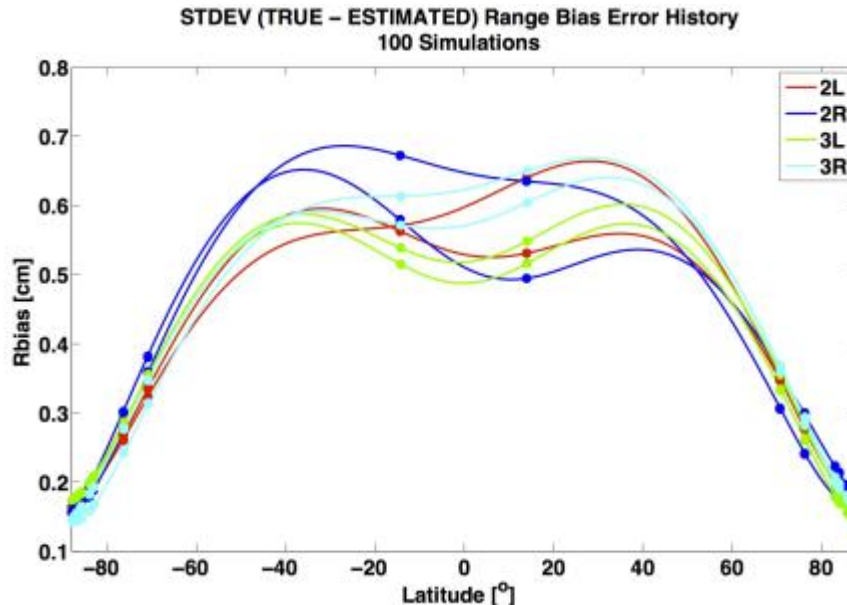
728

729 Analysis of altimetry data during ocean scan maneuvers will be used to calibrate
730 pointing and separate these errors from ranging errors [Luthcke et al., 2000;

731 *Luthcke et al., 2005*]. Ocean scans are routine calibration activities where the
732 instrument will be pointed off-nadir by ≤ 5 degrees and perform conical scans. The
733 expected range bias error is determined from a high fidelity simulation where 10-
734 days of altimeter range cross-over data are simulated between all known and
735 unknown beams including altimeter range observation, orbit and attitude
736 error. The crossovers are then edited to include only cross-overs with less than 1-
737 day of time separation between crossing tracks in order to minimize correlation
738 with geophysical signal. The 1-day binned cross-overs residuals are then reduced
739 formally estimating the range biases for the unknown beams. One hundred
740 simulations are run, each with a new realization of the errors. Figure 9 shows the
741 standard deviation of the difference between the true range biases and the
742 estimated range biases over the 100 simulations as a function of latitude. The range
743 bias error is significantly smaller at high latitudes due to the increased number of
744 crossover observations moving to high latitudes. These simulations suggest a < 5
745 mm range bias calibration error every 10 days for the ice sheets. The long-term drift
746 would be < 1 mm/year.

747

748



749

750 *Fig 9: Potential range bias error (Rbias) as a function of latitude for the beams that
 751 are not monitored by the transmitter echo calibration. This is the residual error after
 752 the calibration.*

753

754 3.4. Geophysical corrections

755

756 The primary measurement of the mission is the photon time of flight from the
 757 satellite to the Earth's surface and back, but most science applications require
 758 converting range into height with respect to a reference ellipsoid. Hence, the
 759 science-directed data products require systematic removal of various geophysical
 760 signals to enhance their scientific usability. Various present-day models of ocean
 761 tides, earth tides, pole tides, dynamic ocean response, and ocean loading, among
 762 other geophysical phenomena are used to determine these geophysical corrections.

763

764 A set of corrections will be applied to the ICESat-2 ATL03 data product (which
765 provides latitude, longitude, and height for each recorded photon event). A design
766 criterion is that these corrections be easily removable for investigations involving
767 improvements to the corrections themselves or for cases when an investigator
768 desires that a different model be applied.

769

770 Ocean tides: Incorporating the assessment by Stammer et al. [2014], ICESat-2 has
771 adopted the GOT4.8 ocean tide model of R. Ray (NASA/GSFC). Over open oceans,
772 ocean tides have typical amplitudes of $\pm 80\text{cm}$, but tides be as large as several meters
773 in coastal and estuary regions as well as under ice shelves.

774

775 Ocean tidal loading: ICESat-2 has adopted loading harmonic grids from the GOT4.8
776 tide model of R. Ray (NASA/GSFC) and include 9 major and 16 minor tidal
777 constituents. Over open oceans, ocean tidal loading amplitudes are on the order of
778 5% of the ocean tide. This correction ranges from -6 to 0 cm.

779

780

781 Solid earth tides: ICESat-2 has adopted the International Earth Rotation and
782 Reference System (IERS) 2010 convention for solid earth tides to take into account
783 the deformation (elastic response) of the solid earth (including the sea floor) due to
784 the attractions of the Sun and Moon. These are applicable globally, and have
785 amplitudes typically on the order of $\pm 40\text{cm}$.

786

787 Dynamic atmospheric correction and inverted barometer effect: ICESat-2 has
788 adopted the utilization of global, empirical, 6-hour, AVISO MOG2D, $1/4^\circ \times 1/4^\circ$ grids
789 to be used as a near-realtime Inverted Barometer (IB) and Dynamic Atmospheric
790 Correction (DAC, *Carrère & Lyard*, 2003). These grids are forced by the European
791 Center for Medium-Range Weather Forecasting (ECMWF) model for the surface
792 pressure and 10m wind fields. This combined correction typically has amplitude on
793 the order of $\pm 50\text{cm}$.

794

795 The range delay through the atmosphere is a function of the total atmospheric
796 pressure, the partial pressure of water vapor and air temperature. Depending on the
797 atmospheric state, this correction is typically between -2.6 and -0.9 m. ICESat-2 uses
798 the output of NASA's Global Modeling and Assimilation Office GEOS-5 model to
799 determine the state of the atmosphere and calculate the total atmospheric range
800 correction.

801

802 Although all heights on ICESat-2 data products are referenced to the WGS-84
803 ellipsoid, there are several science applications that would benefit from the
804 conversion factor between the ellipsoid and the geoid. ICESat-2 provides such a
805 value to allow heights to be converted to the EGM 2008 geoid model in a mean tide
806 system where the permanent tides are included.

807

808 The solid earth and ocean pole tides account for the tidal response of the earth to
809 the centrifugal potential caused by small perturbations of the Earth's rotational axis

810 (i.e. polar motion). The value of these corrections is calculated based on IERS 2010
811 model conventions. Solid earth pole tides have amplitudes typically on the order of
812 $\pm 1.5\text{cm}$ while ocean pole tides have amplitudes typically on the order of $\pm 0.2\text{cm}$.

813

814

815 *Table 2: Summary of auxiliary data and geophysical corrections. The Geoid are*
816 *reference values, but not applied to the product. They are provided for easy*
817 *comparison. The meteorological data are from the atmospheric correction model.*

Model Type	Input Parameters	Output Parameters	Source	Magnitude
Ocean tides	lat, long, time	Ocean height correction	GOT 4.8	$\pm 5 \text{ m}$
Meteorological data	lat, long, time	Surface and column temperature, pressure	NASA GMAO GEOS-5	
Inverted barometer / Dynamic Atmospheric Correction	lat, long, time	Ocean height correction	MOG2D (AVISO)	$\pm 50 \text{ cm}$
Ocean loading	lat, long, time	Ocean height	GOT 4.8	-6 to 0 cm

		correction		
Solid earth pole tide	lat, long, time	Solid earth deformation	IERS Conventions (2010)	±1.5 cm
Ocean pole tide	lat, long, time	Ocean height correction	IERS Conventions (2010)	±0.2 cm
Solid earth tides	lat, long, time	Solid earth deformation	IERS Conventions (2010)	±40 cm
Geoid	lat, long	Reference surface	EGM2008, mean tide system	-105 to +90 m
Total column atmospheric correction	lat, long, time	Range correction	NASA GMAO GEOS-5	-2.6 to -0.9 m

818

819 While several of these geophysical corrections are applied to the photon elevations,
 820 the atmospheric path delay correction is applied during the conversion of photon
 821 time of flight to range. In addition to these operational corrections, scientists may
 822 apply further corrections increasing ICESat-2 precision or accuracy depending on
 823 their discipline.

824

825 3.5 Coverage and operations

826

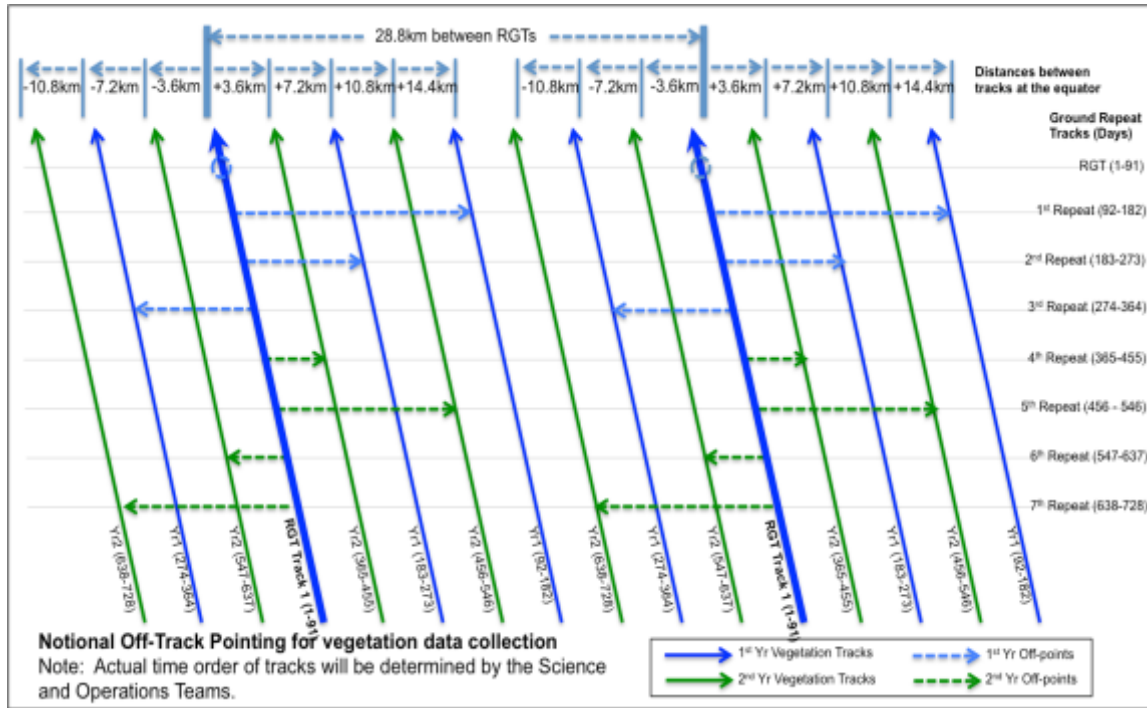
827 ICESat-2 will use a 91-day exact repeat frozen orbit at a 92-degree inclination angle,
828 providing coverage up to 88 degrees North and South generating 1387 ground
829 tracks. It has a nominal orbit altitude of ~500 km. Since the number of ground
830 tracks and the inclination angle are different compared to ICESat, the ICESat-2
831 ground tracks do not align with the ICESat ground tracks. However, there are a
832 substantial number of cross-over locations between the ICESat and ICESat-2 ground
833 tracks, particularly in the polar regions, which will enable linking ICESat-2 data to
834 ICESat.

835

836 ICESat-2 will do repeat-track observations for the polar regions. For mid-latitudes
837 operational off-nadir pointing at different angles will generate a dense grid of
838 measurements over a two-year period. These operational maneuvers are in
839 response to the requirement h) in Section 2 that requires a track density of 2 km
840 over two years. At the equator this leads to the following ground track pattern for
841 the first two years of the mission (Fig. 10). This will enable dense sampling of
842 canopy height measurements and thus provide carbon inventory during the first
843 two years of the mission.

844

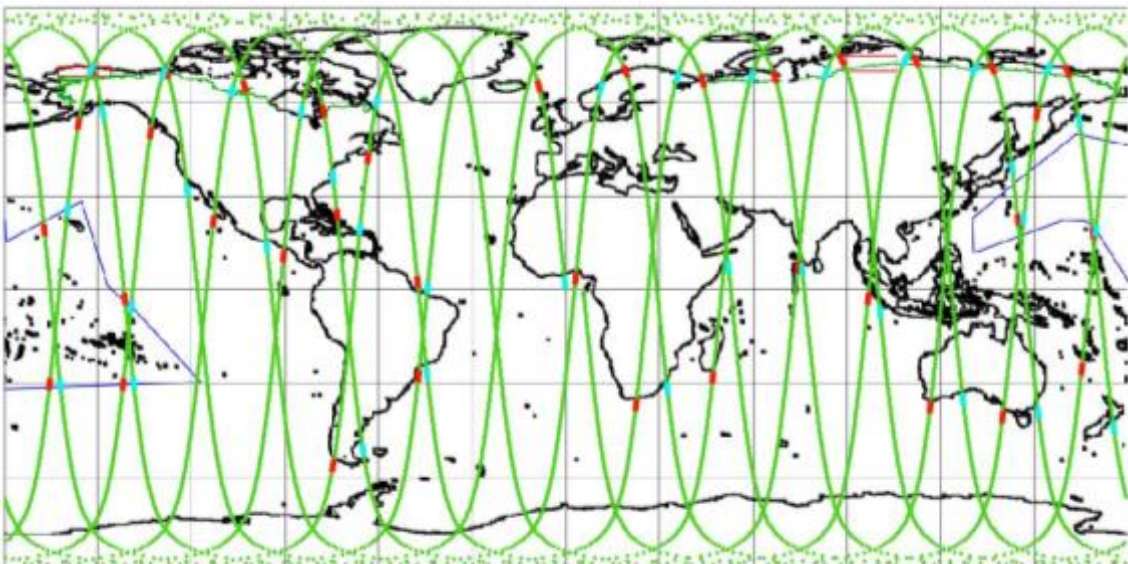
845



846 *Figure 10: Ground track pattern at the equator for the first two years of operation. The bold blue lines show the first tracks for the 2-year period. These are the nominal 91-day repeat tracks. At the equator, the gap is 28.8 km. 91 days later the tracks will be repeated over two years, i.e. 8 times. The combination of ascending and descending orbits will result in track spacings of less than 2 km. The maximum off-nadir angle is about 1.5 degrees.*

853

854 Figure 11 shows one day of reference ground track coverage. The areas in red and
855 blue indicate the transition periods where the satellite changes from the repeat
856 ground track to the “vegetation tracks” and back. Science measurements will be
857 taken at any time during these transitions.



858

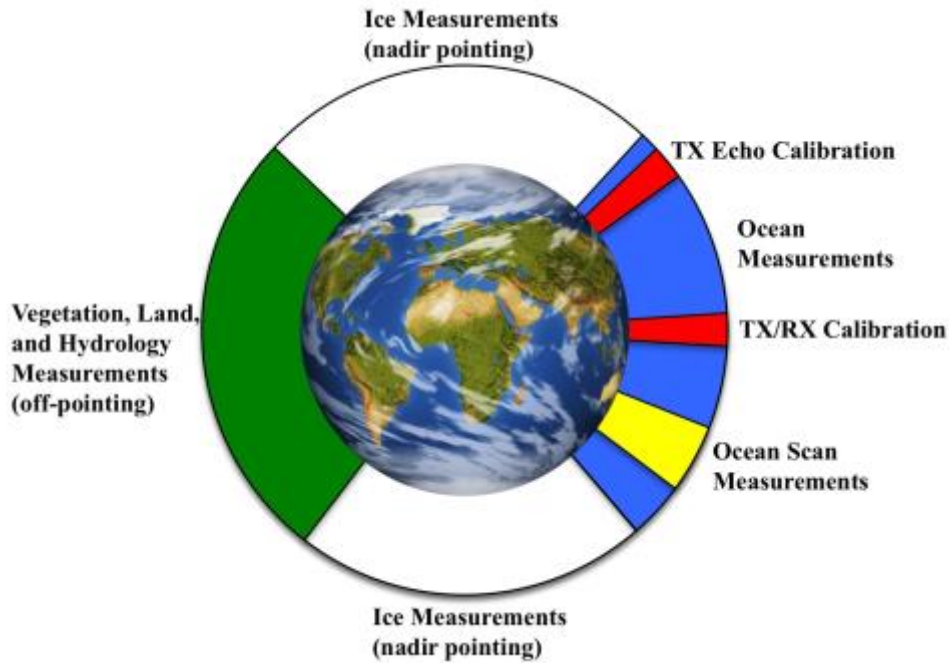
859

860 *Figure 11: Illustration of one day of ICESat-2 orbits. The blue and red orbit sections*
861 *indicate where the pointing transitions from the polar “repeat-track mode” to*
862 *“land/vegetation mode”, respectively. The transition regions have been defined for all*
863 *1387 ground tracks and can be updated on orbit.*

864

865 Figure 12 shows the conceptual mission operations plan. Over the polar regions, the
866 satellite will be in repeat-track mode enabling seasonal repeat measurements. The
867 satellite will point off-nadir over land to generate a dense grid of measurements.
868 While ICESat-2 will generate ocean elevation maps, ICESat-2 will also perform
869 regular calibration maneuvers over the ocean.

870



871

872 *Figure 12: Conceptual mission operations plan. Calibration efforts will be performed*
 873 *over the ocean. TX Echo Calibration refers to Transmit Echo Calibration described in*
 874 *Section 3.3. Ocean Scan Measurements are also described in Section 3.3. TX/RX*
 875 *calibration corrects the set point of the control loop that keeps the transmitted beam*
 876 *aligned to the receiver field of view.*

877

879 **5. Instrument, spacecraft, launch vehicle, ground system**

880

881

882 The ATLAS instrument is being built at NASA Goddard Space Flight Center and will
883 carry two 532 nm lasers, one operating at a time. The laser energy is adjustable and
884 will be between 48 and 170 μJ per pulse with a nominal energy of 120 μJ for the
885 strong spots and a quarter of it for the weak spots. The pulse width of each laser
886 shot is 1.5 ns and the start pulse is timed at four points over the transmit waveform.

887 Generally the start time will be the average of these four times but the separate
888 measurements allow the monitoring of changes in pulse width and pulse shape
889 symmetry. At the focal plane of the 0.8 m diameter telescope are 6 receiver fibers
890 that send the light through a very narrow (+-19 pm) filter to eliminate most of the
891 sunlight. The remaining photons are then detected by photo-multiplier tubes.

892 ATLAS carries a redundant bank of detectors. More ATLAS parameters are provided
893 in Appendix A.

894

895 The spacecraft is being built by Orbital ATK in Gilbert, AZ, and utilizes the heritage
896 from the Landsat-8 satellite, which was also built by Orbital ATK. The spacecraft will
897 carry fuel for a 7-year mission. To enable the required high precision orbit and
898 pointing knowledge the GPS system and star trackers are directly mounted onto the
899 ATLAS optical bench instead of on the spacecraft.

900

901 The ICESat-2 Observatory will be launched on board a United Launch Alliance (ULA)

902 Delta II 7420-10 launch vehicle at Vandenberg Air Force Base. The ICESat-2 mission
903 will be the final launch for the Delta II program after more than 150 launches dating
904 back to 1989.

905

906 The Mission Operation Center (MOC) will be in Reston, VA with a back-up MOC in
907 Gilbert, AZ. The MOC performs observatory commanding and monitoring
908 throughout the mission lifespan. This includes mission planning and scheduling,
909 monitor and control of the spacecraft, controlling ground communications, and
910 maintaining spacecraft flight software. NASA Goddard Space Flight Center is hosting
911 the Instrument Support Facility (ISF) and the Science Investigator-led Processing
912 System (SIPS). The ISF performs ATLAS mission planning, command, and control,
913 ATLAS health and safety monitoring, and trend analysis of ATLAS operations. It
914 maintains ATLAS flight software and configuration. The SIPS will provide the
915 functions necessary to produce and distribute the routine science products for the
916 ICESat-2 mission. A complete list of data products is given in Appendix B. Data
917 products will be sent from the SIPS to the NASA Distributed Active Archive Center
918 (DAAC) at the National Snow and Ice Date Center in Boulder, CO for distribution to
919 the public. The data latency is 2 weeks for the geolocated range and elevation data,
920 and 1 month for the geophysical data after completion of data accumulation
921 required for the specific geophysical products.

922

923 **6. Summary**

924

925 ICESat-2 is a 2nd generation space laser altimeter for earth elevation measurements
926 and differs substantially from its ICESat predecessor in concept, technology, data
927 products, and operations compared to ICESat. Lessons learned and scientific
928 findings from ICESat were considered in the design and development of ICESat-2.

929

930 The multi-beam approach is central to ICESat-2. This will enable the separation of
931 slope effects from elevation changes on a track-by-track basis and will enable the
932 retrieval of ice sheet elevation changes on a seasonal basis. Given that ICESat
933 operated in 30-day campaign mode, ICESat-2's three pairs of beams, together with
934 the planned continuous operation, will result in 9 times better coverage.

935 Furthermore, the footprint size and footprint spacing are significantly smaller to
936 optimize elevation retrievals over heterogeneous glaciers and to optimize sea
937 surface height estimates from the, often narrow, leads to enable sea ice freeboard
938 retrievals. Operational off-nadir pointing over land areas will ensure optimum
939 coverage for terrestrial and vegetation sciences. ICESat-2 will be the first time that a
940 photon counting laser altimeter concept is realized on a space-borne platform.

941

942 **Appendix A:**

943

944 List of key mission parameters

945

946 Observatory:

947

Orbit inclination and coverage	92 degrees; coverage up to 88 degrees N and S
Track repeat period (polar regions)	91-day exact repeat orbit with monthly sub-cycle for the polar regions and oceans. Operational off-nadir pointing over land areas to generate a dense grid of data over 2 years.
Nominal altitude	500 km
Semi-major axis	6855.9539 km
Pointing control	45 m
Pointing knowledge	6.5 m
Nominal duration of mission	3 years

948

949 ATLAS:

950

951

Laser wavelength	532 nm
Transmitted pulse width	1.5 ns FWHM
Pulse repetition rate	10 kHz (~0.7 m along-track spacing at nominal altitude)
Number of beams	6 organized in 3 pairs
Beam spacing (across track) at nominal altitude	90 m within pairs 3.3 km between pairs
Illuminated spot diameter (85% EE)	<17.5 m at nominal altitude
Telescope aperture diameter	0.8 m
Receiver field of view diameter	42.5 m at nominal altitude
Solar-blocking filter effective width	38 pm
Photon-counting detector	Hamamatsu photomultiplier with 16 detector elements for strong beams and 4 detector elements for weak beams
Receiver dead time, per channel	3.2 ± 0.2 ns
Single photon time-of-flight precision	800 ps (standard deviation)

952

953 MABEL:

954

Laser wavelength	532 and 1064 nm
Transmitted pulse width	1.5 ns
ER-2 nominal altitude	~20 km (65,000 ft)
Pulse repetition rate	5 – 25 kHz; operated at 5 kHz (~0.04 m along-track spacing at nominal altitude)
Number of beams	As many as 16 (532 nm) and 8 (1064 nm) beams organized into 2 linear arrays
Total ground swath	~2 km
Footprint size	2 m (at nominal altitude)
Telescope aperture diameter	0.13 m
Receiver field of view diameter	2 m (at nominal altitude)
Photon-counting detector	Hamamatsu model H7260 photomultiplier
Receiver dead time	3 ns
Single photon time-of-flight precision	800 ps (standard deviation)

955

956

957

958 **Appendix B:**

959

960 *Overview of the operational ICESat-2 data products. The left column contains the*
 961 *product indicator name.*

ATL00	Telemetry Data	Raw ATLAS telemetry in packet format
ATL01	Reformatted Telemetry	Parsed, partially reformatted into HDF5, generated daily, segmented into several minute granules.
ATL02	Science Unit Converted Telemetry	Photon time of flight, corrected for instrument effects. Includes all photons, pointing data, spacecraft position, housekeeping data, engineering data, and raw atmospheric profiles, segmented into several minute granules.
ATL03	Global Geolocated Photon Data	Precise latitude, longitude and elevation for every received photon, arranged by beam in the along-track direction. Photons classified by signal vs. background, as well as by surface type (land ice, sea ice, land, ocean), including all geophysical corrections (e.g. Earth tides, atmospheric delay, etc...). Segmented into several minute granules.
ATL04	Uncalibrated Backscatter Profiles	Along-track atmospheric backscatter data, 25 times per second. Includes calibration coefficients for polar regions. Segmented into several minute granules.
ATL06	Land Ice Elevation	Surface height for each beam with along- and across-track slopes

		calculated for each beam pair. Posted at 40m along-track; segmented into several minute granules.
ATL07	Arctic/Antarctic Sea Ice Elevation	Height of sea ice and open water leads at varying length scale based on returned photon rate for each beam presented along-track.
ATL08	Land Water Vegetation Elevation	Height of ground including canopy surface posted at variable length scales relative to signal level, for each beam presented along-track. Where data permits include canopy height, canopy cover percentage, surface slope and roughness, and apparent reflectance.
ATL09	Calibrated Backscatter and Cloud Characteristics	Along-track cloud and other significant atmosphere layer heights, blowing snow, integrated backscatter, and optical depth.
ATL10	Arctic/Antarctic Sea Ice Freeboard	Estimate of sea ice freeboard over specific spatial scales using all available sea surface height measurements. Contains statistics of sea surface and sea ice heights.
ATL11	Antarctica / Greenland Ice Sheet H(t) Series	Time series of height at points on the ice sheet, calculated based on repeat tracks and/or cross-overs.
ATL12	Ocean Elevation	Surface height at specific length scale. Where data permits include estimates of height distribution, roughness, surface slope, and apparent reflectance.
ATL13	Inland Water Height	Along-track inland and near shore water surface height distribution within water mask. Where data permit, include roughness, slope and aspect

ATL14	Antarctica / Greenland Ice Sheet H(t) Gridded	Height maps of each ice sheet for each year based on all available elevation data.
ATL15	Antarctica / Greenland Ice Sheet dh/dt Gridded	Height change maps for each ice sheet, for each mission year, and for the whole mission.
ALT16	ATLAS Atmosphere Weekly	Polar cloud fraction, blowing snow frequency, ground detection frequency.
ATL17	ATLAS Atmosphere Monthly	Polar cloud fraction, blowing snow frequency, ground detection frequency.
ATL18	Land/Canopy Gridded	Gridded ground surface height, canopy height, and canopy cover estimates.
ATL19	Mean Sea Surface (MSS)	Gridded ocean height product.
ATL20	Arctic / Antarctic Gridded Sea Ice Freeboard	Gridded sea ice freeboard.
ATL21	Arctic/Antarctic Gridded Sea Surface Height w/in Sea Ice	Gridded monthly sea surface height inside the sea ice cover.

962

963

964 **References**

- 965 Abdalati, W., Zwally, H. J., Bindschadler, R., Csatho, B., Farrell, S. L., Fricker, H. A.,
966 Harding, D., Kwok, R., Lefsky, M., Markus, T., Marshak, A., Neumann, T., Palm,
967 S., Schutz, B., Smith, B., Spinhirne, J., & Webb, C. (2010). The ICESat-2 laser
968 altimetry mission. *Proceedings of the IEEE*, 98(5), 735-751, doi:
969 10.1109/JPROC.2009.2034765.
- 970
- 971 Bolch, T., Sandberg Sørensen, L., Simonsen, S. B., Mölg, N., Machguth, H., Rastner, P.,
972 & Paul, F. (2013). Mass loss of Greenland's glaciers and ice caps 2003–2008
973 revealed from ICESat laser altimetry data. *Geophysical Research Letters*,
974 40(5), 875-881, doi: 10.1002/grl.50270.
- 975
- 976 Brunt, K. M., Fricker, H. A., Padman, L., Scambos, T. A., & O'Neil, S. (2010). Mapping
977 the grounding zone of the Ross Ice Shelf, Antarctica, using ICESat laser
978 altimetry. *Annals of Glaciology*, 51(55), 71-79, doi:
979 10.3189/172756410791392790
- 980
- 981 Brunt, K. M., Fricker, H. A., & Padman, L. (2011). Analysis of ice plains of the
982 Filchner–Ronne Ice Shelf, Antarctica, using ICESat laser altimetry. *Journal of
983 Glaciology*, 57(205), 965-975, doi: 10.3189/002214311798043753.
- 984
- 985 Brunt, K. M., Neumann, T. A., Walsh, K. M., & Markus, T. (2014). Determination of
986 local slope on the Greenland Ice Sheet using a multibeam photon-counting

- 987 Lidar in preparation for the ICESat-2 Mission. Geoscience and Remote
988 Sensing Letters, IEEE, 11(5), 935-939, doi: 10.1109/LGRS.2013.2282217.
- 989
- 990 Brunt, K. M., Neumann, T. A., Amundson, J. M., Kavanaugh, J. L., Moussavi, M. S.,
991 Walsh, K. M., Cook, W. B., & Markus, T. (2016). MABEL photon-counting laser
992 altimetry data in Alaska for ICESat-2 simulations and development. The
993 Cryosphere Discussions, 1–31, doi: 10.5194/tc-2015-225.
- 994
- 995 Connor, L. N., Farrell, S. L., McAdoo, D. C., Krabill, W. B., & Manizade, S. (2013).
996 Validating icesat over thick sea ice in the northern canada basin. Geoscience
997 and Remote Sensing, IEEE Transactions on, 51(4), 2188-2200,
998 doi:10.1109/TGRS.2012.2211603.
- 999
- 1000 Csatho, B. M., Schenk, A. F., van der Veen, C. J., Babonis, G., Duncan, K.,
1001 Rezvanbehbahani, S., van den Broeke, M. R., Simonsen, S. B., Nagarajan, S., &
1002 van Angelend, J. H. (2014). Laser altimetry reveals complex pattern of
1003 Greenland Ice Sheet dynamics. Proceedings of the National Academy of
1004 Sciences, 111(52), 18478-18483, doi: 10.1073/pnas.1411680112.
- 1005
- 1006 Farrell, S. L., Brunt, K. M., Ruth, J. M., Kuhn, J. M., Connor, L. N., & Walsh, K. M. (2015).
1007 Sea-ice freeboard retrieval using digital photon-counting laser altimetry.
1008 Annals of Glaciology, 56(69), 167-174, doi: 10.3189/2015AoG69A686.
- 1009

- 1010 Farrell, S. L., Laxon, S. W., McAdoo, D. C., Yi, D., & Zwally, H. J. (2009). Five years of
1011 Arctic sea ice freeboard measurements from the Ice, Cloud and land
1012 Elevation Satellite. *Journal of Geophysical Research: Oceans*, 114(C4), doi:
1013 10.1029/2008JC005074.
- 1014
- 1015 Farrell, S. L., McAdoo, D. C., Laxon, S. W., Zwally, H. J., Yi, D., Ridout, A., & Giles, K.
1016 (2012). Mean dynamic topography of the Arctic Ocean. *Geophysical Research
Letters*, 39(1), doi: 10.1029/2011GL050052.
- 1018
- 1019 Fricker, H. A., Scambos, T., Bindschadler, R., & Padman, L. (2007). An active
1020 subglacial water system in West Antarctica mapped from space. *Science*,
1021 315(5818), 1544-1548, doi: 10.1126/science.1136897.
- 1022
- 1023 Fricker, H. A., Coleman, R., Padman, L., Scambos, T. A., Bohlander, J., & Brunt, K. M.
1024 (2009). Mapping the grounding zone of the Amery Ice Shelf, East Antarctica
1025 using InSAR, MODIS and ICESat. *Antarctic Science*, 21(05), 515-532, doi:
1026 10.1017/S095410200999023X.
- 1027
- 1028 Gardner, A., Moholdt, G., Arendt, A., & Wouters, B. (2012). Accelerated contributions
1029 of Canada's Baffin and Bylot Island glaciers to sea level rise over the past half
1030 century. *The Cryosphere*, 6(5), 1103-1125, doi:10.5194/tc-6-1103-2012.
- 1031
- 1032 Gardner, A. S., Moholdt, G., Cogley, J. G., Wouters, B., Arendt, A. A., Wahr, J., Berthier,

- 1033 E., Hock, R., Pfeffer, W. T., Kaser, G., Ligtenberg, S. R. M., Bolch, T., Sharp, M. J.,
- 1034 Hagen, J. O., van den Broeke, M. R., & Paul, F. (2013). A reconciled estimate of
- 1035 glacier contributions to sea level rise: 2003 to 2009. *Science*, 340(6134), 852-
- 1036 857, doi: 10.1126/science.1234532.
- 1037
- 1038 Gardner, A. S., Moholdt, G., Wouters, B., Wolken, G. J., Burgess, D. O., Sharp, M. J.,
- 1039 Cogley, J. G., Braun, C., & Labine, C. (2011). Sharply increased mass loss from
- 1040 glaciers and ice caps in the Canadian Arctic Archipelago. *Nature*, 473(7347),
- 1041 357-360, doi: 10.1038/nature10089.
- 1042
- 1043 Glenn, N. F., Neuenschwander, A., Vierling, L. A., Spaete, L., Li, A., Shinneman, D. J.,
- 1044 Pilliod, D. S., Arkle, R. S., & McIlroy, S. K. (2016). Landsat 8 and ICESat-2:
- 1045 Performance and potential synergies for quantifying dryland ecosystem
- 1046 vegetation cover and biomass. *Remote Sensing of Environment*, doi:
- 1047 10.1016/j.rse.2016.02.039.
- 1048
- 1049 Groh, A., Ewert, H., Scheinert, M., Fritsche, M., Rülke, A., Richter, A., Rosenau, R., &
- 1050 Dietrich, R. (2012). An investigation of glacial isostatic adjustment over the
- 1051 Amundsen Sea Sector, West Antarctica. *Global and Planetary Change*, 98, 45-
- 1052 53, doi: 10.1016/j.gloplacha.2012.08.001.
- 1053
- 1054 Gunter, B., Urban, T., Riva, R., Helsen, M., Harbold, R., Poole, S., Nagel, P., Schutz, B., &
- 1055 Tapley, B. (2009). A comparison of coincident GRACE and ICESat data over

1056 Antarctica. Journal of Geodesy, 83(11), 1051-1060, doi: 10.1007/s00190-
1057 009-0323-4.
1058
1059 Gwenzi, D., & Lefsky, M. A. (2014). Prospects of photon counting lidar for savanna
1060 ecosystem structural studies. The International Archives of Photogrammetry,
1061 Remote Sensing and Spatial Information Sciences, 40(1), 141, doi:
1062 10.5194/isprsarchives-XL-1-141-2014.
1063
1064 Haran, T., Bohlander, J., Scambos, T., & Fahnestock, M. (2005). compilers: MODIS
1065 mosaic of Antarctica (MOA) image map: Digital media. National Snow and Ice
1066 Data Center, Boulder, CO, USA.
1067
1068 Harding, D. J., & Carabajal, C. C. (2005). ICESat waveform measurements of within -
1069 footprint topographic relief and vegetation vertical structure. Geophysical
1070 research letters, 32(21), doi: 10.1029/2005GL023971.
1071
1072 Hay, C. C., Morrow, E., Kopp, R. E., & Mitrovica, J. X. (2015). Probabilistic reanalysis of
1073 twentieth-century sea-level rise. Nature, 517(7535), 481-484, doi:
1074 10.1038/nature14093.
1075
1076 Herzfeld, U. C., McDonald, B. W., Wallin, B. F., Neumann, T. A., Markus, T., Brenner, A.,
1077 & Field, C. (2014). Algorithm for detection of ground and canopy cover in
1078 micropulse photon-counting lidar altimeter data in preparation for the

- 1079 ICESat-2 mission. Geoscience and Remote Sensing, IEEE Transactions on,
1080 52(4), 2109-2125, doi: 10.1109/TGRS.2013.2258350.
- 1081
- 1082 Houghton, R. A. (2005). Aboveground forest biomass and the global carbon balance.
1083 Global Change Biology, 11(6), 945-958, doi: 10.1111/j.1365-
1084 2486.2005.00955.x.
- 1085
- 1086 Howat, I. M., Smith, B. E., Joughin, I., & Scambos, T. A. (2008). Rates of southeast
1087 Greenland ice volume loss from combined ICESat and ASTER observations.
1088 Geophysical Research Letters, 35(17), doi: 10.1029/2008gl034496.
- 1089
- 1090 Jasinski, M. F., Stoll, J. D., Cook, W. B., Ondrusek, M., Stengel, E., & Brunt, K.M. (2016,
1091 accepted). Inland and near shore water profiles derived from the high
1092 altitude Multiple Altimeter Beam Experimental Lidar (MABEL). Journal of
1093 Coastal Research.
- 1094
- 1095 Kääb, A., Berthier, E., Nuth, C., Gardelle, J., & Arnaud, Y. (2012). Contrasting patterns
1096 of early twenty-first-century glacier mass change in the Himalayas. Nature,
1097 488(7412), 495-498, doi: 10.1038/nature11324
- 1098
- 1099 Khan, S. A., Kjær, K. H., Bevis, M., Bamber, J. L., Wahr, J., Kjeldsen, K. K., Bjørk, A. A.,
1100 Korsgaard, N. J., Stearns, L. A., van den Broeke, M. R., Liu, L., Larsen, N. K., &
1101 Muresan, J. S. (2014). Sustained mass loss of the northeast Greenland ice

sheet triggered by regional warming. *Nature Climate Change*, 4(4), 292-299,
doi: 10.1038/nclimate2161.

Krankina, O. N., Harmon, M. E., Schnekenburger, F., & Sierra, C. A. (2012). Carbon
balance on federal forest lands of Western Oregon and Washington: the
impact of the Northwest Forest Plan. *Forest Ecology and Management*, 286,
171-182.

Kuipers Munneke, P., Ligtenberg, S., Noël, B. P. Y., Howat, I. M., Box, J. E., Mosley-
Thompson, E., McConnell, J. R.; Steffen, K., Harper, J. T., Das, S. B., & Van Den
Broeke, M. R. (2015). Elevation change of the Greenland Ice Sheet due to
surface mass balance and firn processes, 1960-2014. *The Cryosphere*, 9(6),
2009-2025, doi: 10.5194/tc-9-2009-2015

Kurtz, N. T., & Markus, T. (2012). Satellite observations of Antarctic sea ice thickness
and volume. *Journal of Geophysical Research: Oceans*, 117(C8), doi:
10.1029/2012JC008141.

Kwok, R., Cunningham, G. F., Wensnahan, M., Rigor, I., Zwally, H. J., & Yi, D. (2009).
Thinning and volume loss of the Arctic Ocean sea ice cover: 2003–2008.
Journal of Geophysical Research: Oceans, 114(C7),
doi:10.1029/2009JC005312.

- 1125 Kwok, R., & Rothrock, D. A. (2009). Decline in Arctic sea ice thickness from
1126 submarine and ICESat records: 1958–2008. *Geophysical Research Letters*,
1127 36(15), doi:10.1029/2009GL039035.
- 1128
- 1129 Kuipers Munneke, P., Ligtenberg, S., Noël, B. P. Y., Howat, I. M., Box, J. E., Mosley-
1130 Thompson, E., McConnell, J. R.; Steffen, K., Harper, J. T., Das, S. B., & Van Den
1131 Broeke, M. R. (2015). Elevation change of the Greenland Ice Sheet due to
1132 surface mass balance and firn processes, 1960-2014. *The Cryosphere*, 9(6),
1133 2009-2025, doi: 10.5194/tc-9-2009-2015
- 1134
- 1135 Laxon, S. W., Giles, K. A., Ridout, A. L., Wingham, D. J., Willatt, R., Cullen, R., Kwok, R.,
1136 Schweiger, A., Zhang, J., Haas, C., Hendricks, S., Krishfield, R., Kurtz, N., Farrell,
1137 S. L., & Davidson, M. (2013). CryoSat - 2 estimates of Arctic sea ice thickness
1138 and volume. *Geophysical Research Letters*, 40(4), 732-737, doi:
1139 10.1002/grl.50193.
- 1140
- 1141 Le Quéré, C., et al. (2015). Global carbon budget 2014, doi: 10.5194/essd-7-47-2015
- 1142
- 1143 Lefsky, M. A., Keller, M., Pang, Y., De Camargo, P. B., & Hunter, M. O. (2007). Revised
1144 method for forest canopy height estimation from Geoscience Laser Altimeter
1145 System waveforms. *Journal of Applied Remote Sensing*, 1(1), 013537-013537,
1146 doi: 10.1117/1.2795724.
- 1147

- 1148 Lefsky, M. A. (2010). A global forest canopy height map from the Moderate
1149 Resolution Imaging Spectroradiometer and the Geoscience Laser Altimeter
1150 System. *Geophysical Research Letters*, 37(15), doi: 10.1029/2010GL043622.
- 1151
- 1152 Ligtenberg, S. R. M., Horwath, M., den Broeke, M. R., & Legrésy, B. (2012).
1153 Quantifying the seasonal “breathing” of the Antarctic ice sheet. *Geophysical*
1154 *Research Letters*, 39(23), doi: 10.1029/2012GL053628.
- 1155
- 1156 Los, S. O., Rosette, J. A. B., Kljun, N., North, P. R. J., Chasmer, L., Suárez, J. C., Hopkinson,
1157 C., Hill, R. A., van Gorsel, E., Mahoney, C., & Berni, J. A. J. (2012). Vegetation
1158 height and cover fraction between 60 S and 60 N from ICESat GLAS data.
1159 *Geoscientific Model Development*, 5(2), 413-432, doi: 10.5194/gmd-5-413-
1160 2012.
- 1161
- 1162 Luthcke, S. B., Rowlands, D. D., McCarthy, J. J., Pavlis, D. E., & Stoneking, E. (2000).
1163 Spaceborne laser-altimeter-pointing bias calibration from range residual
1164 analysis. *Journal of Spacecraft and Rockets*, 37(3), 374-384, doi:
1165 10.2514/2.3571.
- 1166
- 1167 Luthcke, S. B., Rowlands, D. D., Williams, T. A., & Sirota, M. (2005). Reduction of
1168 ICESat systematic geolocation errors and the impact on ice sheet elevation
1169 change detection. *Geophysical research letters*, 32(21), doi:
1170 10.1029/2005GL023689.

1171
1172 Luthcke, S.B., T.J. Sabaka, B.D. Loomis, A.A. Arendt, J.J. McCarthy, J. Camp (2013),
1173 Antarctica, Greenland and Gulf of Alaska land ice evolution from an iterated
1174 GRACE global mascon solution, *J. Glac.*, 59(216),
1175 doi:10.3189/2013jJoG12j147.
1176
1177 Loomis, B.D. and S.B. Luthcke (2014), Optimized signal denoising and adaptive
1178 estimation of seasonal timing and mass balance from simulated GRACE-like
1179 regional mass variations, *Adv. In Adap. Data Anal.*, 6(1), doi:
1180 10.1142/S1793536914500034.
1181
1182 McAdoo, D. C., Farrell, S. L., Laxon, S., Ridout, A., Zwally, H. J., & Yi, D. (2013). Gravity
1183 of the Arctic Ocean from satellite data with validations using airborne
1184 gravimetry: oceanographic implications. *Journal of Geophysical Research: Oceans*, 118(2), 917-930, doi: 10.1002/jgrc.20080.
1186
1187 McGill, M., Markus, T., Scott, V. S., & Neumann, T. (2013). The multiple altimeter
1188 beam experimental Lidar (MABEL): An airborne simulator for the ICESat-2
1189 mission. *Journal of Atmospheric and Oceanic Technology*, 30(2), 345-352,
1190 doi: 10.1175/JTECH-D-12-00076.1.
1191
1192 Moholdt, G., Nuth, C., Hagen, J. O., & Kohler, J. (2010). Recent elevation changes of
1193 Svalbard glaciers derived from ICESat laser altimetry. *Remote Sensing of*

1194 Environment, 114(11), 2756-2767, doi: 10.1016/j.rse.2010.06.008.
1195
1196 Moholdt, G., Wouters, B., & Gardner, A. S. (2012). Recent mass changes of glaciers in
1197 the Russian High Arctic. Geophysical Research Letters, 39(10), doi:
1198 10.1029/2012gl051466.
1199
1200 Neuenschwander, A. L., Urban, T. J., Gutierrez, R., & Schutz, B. E. (2008).
1201 Characterization of ICESat/GLAS waveforms over terrestrial ecosystems:
1202 Implications for vegetation mapping. Journal of Geophysical Research:
1203 Biogeosciences, 113(G2), doi: 10.1029/2007JG000557
1204
1205 Padman, L., Erofeeva, S. Y., & Fricker, H. A. (2008). Improving Antarctic tide models
1206 by assimilation of ICESat laser altimetry over ice shelves. Geophysical
1207 Research Letters, 35(22), doi: 10.1029/2008GL035592.
1208
1209 Price, S. F., Payne, A. J., Howat, I. M., & Smith, B. E. (2011). Committed sea-level rise
1210 for the next century from Greenland ice sheet dynamics during the past
1211 decade. Proceedings of the National Academy of Sciences, 108(22), 8978-
1212 8983, doi: 10.1073/pnas.1017313108.
1213
1214 Pritchard, H. D., Arthern, R. J., Vaughan, D. G., & Edwards, L. A. (2009). Extensive
1215 dynamic thinning on the margins of the Greenland and Antarctic ice sheets.
1216 Nature, 461(7266), 971-975, doi:10.1038/nature08471.

- 1217
- 1218 Pritchard, H. D., Ligtenberg, S. R. M., Fricker, H. A., Vaughan, D. G., Van den Broeke, M.
- 1219 R., & Padman, L. (2012). Antarctic ice-sheet loss driven by basal melting of ice
- 1220 shelves. *Nature*, 484(7395), 502-505, doi: 10.1038/nature10968.
- 1221
- 1222 Ray, R. D. (2008). A preliminary tidal analysis of ICESat laser altimetry: Southern
- 1223 Ross Ice Shelf. *Geophysical Research Letters*, 35(2), doi:
- 1224 10.1029/2007GL032125
- 1225
- 1226 Rothrock, D. A., Percival, D. B., & Wensnahan, M. (2008). The decline in arctic sea -
- 1227 ice thickness: Separating the spatial, annual, and interannual variability in a
- 1228 quarter century of submarine data. *Journal of Geophysical Research: Oceans*,
- 1229 113(C5), doi: 10.1029/2007JC004252.
- 1230
- 1231 Sasgen, I., van den Broeke, M., Bamber, J. L., Rignot, E., Sørensen, L. S., Wouters, B.,
- 1232 Martinech, Z., Velicogna, I., & Simonsen, S. B. (2012). Timing and origin of
- 1233 recent regional ice-mass loss in Greenland. *Earth and Planetary Science*
- 1234 *Letters*, 333, 293-303, doi: 10.1016/j.epsl.2012.03.033.
- 1235
- 1236 Shepherd, A., Ivins, E. R., A, G., Barletta, V. R., Bentley, M. J., Bettadpur, S., Briggs, K. H.,
- 1237 Bromwich, D. H., Forsberg, R., Galin, N., Horwath, M., Jacobs, S., Joughin, I.,
- 1238 King, M. A., Lenaerts, J. T. M., Li, J., Ligtenberg, S. R. M., Luckman, A., Luthcke, S.
- 1239 B., McMillan, M., Meister, R., Milne, G., Mouginot, J., Muir, A., Nicolas, J. P.,

- 1240 Paden, J., Payne, A. J., Pritchard, H., Rignot, E., Rott, H., Sorensen, L. S.,
1241 Scambos, T. A., Scheuchl, B., Schrama, E. J. O., Smith, B., Sundal, A. V., van
1242 Angelen, J. H., van de Berg, W. J., van den Broeke, M. R., Vaughan, D. G.,
1243 Velicogna, I., Wahr, J., Whitehouse, P. L., Wingham, D. J., Yi, D., Young, D., &
1244 Zwally, H. J., 2012. A reconciled estimate of ice-sheet mass balance. *Science*,
1245 338(6111), 1183-1189, doi: 10.1126/science.1228102.
- 1246
- 1247 Schutz, B. E., Zwally, H. J., Shuman, C. A., Hancock, D., & DiMarzio, J. P. (2005).
1248 Overview of the ICESat mission. *Geophysical Research Letters*, 32(21), doi:
1249 10.1029/2005GL024009.
- 1250
- 1251 Simard, M., Pinto, N., Fisher, J. B., & Baccini, A. (2011). Mapping forest canopy height
1252 globally with spaceborne lidar. *Journal of Geophysical Research:*
1253 *Biogeosciences*, 116(G4), doi: 10.1029/2011JG001708.
- 1254
- 1255 Smith, B. E., Fricker, H. A., Joughin, I. R., & Tulaczyk, S. (2009). An inventory of active
1256 subglacial lakes in Antarctica detected by ICESat (2003–2008). *Journal of*
1257 *Glaciology*, 55(192), 573-595, doi: 10.3189/002214309789470879.
- 1258
- 1259 Sørensen, L.S., Simonsen, S. B., Nielsen, K., Lucas-Picher, P., Spada, G., Adalgeirsdottir,
1260 G., Forsberg, R., & Hvidberg, C. (2011). Mass balance of the Greenland ice
1261 sheet (2003–2008) from ICESat data—the impact of interpolation, sampling
1262 and firn density. *The Cryosphere*, 5, 173-186, doi: 10.5194/tc-5-173-2011.

- 1263
- 1264 Spinhirne, J. D., Palm, S. P., Hart, W. D., Hlavka, D. L., & Welton, E. J. (2005). Cloud and
1265 aerosol measurements from GLAS: Overview and initial results. *Geophysical
1266 Research Letters*, 32(22), doi: 10.1029/2005GL023507.
- 1267
- 1268 Stammer, D., Ray, R. D., Andersen, O. B., Arbic, B. K., Bosch, W., Carrère, L., Cheng, Y.,
1269 Chinn, D. S., Dushaw, B. D., Egbert, G. D., Erofeeva, S. Y., Fok, H. S., Green, J. A.
1270 Griffiths, S., King, M. A., Lapin, V., Lemoine, F. G., Luthcke, S. B., Lyard, F.,
1271 Morison, J., Müller, M., Padman, L., Richman, J. G., Shriver, J. F., Shum, C. K.,
1272 Taguchi, E., & Yi, Y. (2014). Accuracy assessment of global barotropic ocean
1273 tide models. *Reviews of Geophysics*, 52(3), 243-282, doi:
1274 10.1002/2014RG000450.
- 1275
- 1276 Stamnes, K., Tsay, S. C., Wiscombe, W., & Jayaweera, K. (1988). Numerically stable
1277 algorithm for discrete-ordinate-method radiative transfer in multiple
1278 scattering and emitting layered media. *Applied optics*, 27(12), 2502-2509,
1279 doi: 10.1364/AO.27.002502.
- 1280
- 1281 Thomas, R., Frederick, E., Krabill, W., Manizade, S., & Martin, C. (2009). Recent
1282 changes on Greenland outlet glaciers. *Journal of Glaciology*, 55(189), 147-162,
1283 doi: 10.3189/002214309788608958.
- 1284
- 1285 Urban, T. J., & Schutz, B. E. (2005). ICESat sea level comparisons. *Geophysical*

1286 research letters, 32(23), doi: 10.1029/2005GL024306.

1287

1288 Urban, T. J., Schutz, B. E., & Neuenschwander, A. L. (2008). A Survey of ICESat Coastal
1289 Altimetry Applications: Continental Coast, Open Ocean Island, and Inland
1290 River. *Terrestrial, Atmospheric & Oceanic Sciences*, 19, doi:
1291 10.3319/TAO.2008.19.1-2.1(SA).

1292

1293 Zwally, H. J., Jun, L. I., Brenner, A. C., Beckley, M., Cornejo, H. G., DiMarzio, J.,
1294 Giovinetto, M. B., Neumann, T. A., Robbins, J., Saba, J. L., Yi, D., Wang, W.
1295 (2011). Greenland ice sheet mass balance: distribution of increased mass loss
1296 with climate warming; 2003–07 versus 1992–2002. *Journal of Glaciology*,
1297 57(201), 88–102, doi: 10.3189/002214311795306682.

1298

1299 Zwally, H. J., Li, J., Robbins, J. W., Saba, J. L., Yi, D., & Brenner, A. C. (2015). Mass gains
1300 of the Antarctic ice sheet exceed losses. *Journal of Glaciology*, 61(230), 1019–
1301 1036, doi: 10.3189/2015JoG15J071.

1302

1303

1304 Figure Captions:

1305

1306 *Figure 1:*

1307 *Greenland ice sheet cumulative mass change time series from NASA GSFC mascon
1308 solution (update to Luthcke et al., 2013). Mascon solution shown as dashed line with
1309 Ensemble Empirical Mode Decomposition (EEMD) filtered mascon solution time series
1310 as solid line with seasonal minima determined from EEMD analysis (Loomis and
1311 Luthcke, 2014)). Significant inter-annual variations are observed including the
1312 extreme summer mass loss in 2012 followed by the recent pause in mass loss.*

1313

1314 *Figure 2:*

1315 *ICESat-2's sampling geometry. The beam pattern is a 3 x 2 array that, by slightly
1316 yawing the spacecraft, creates three pairs of beams on the ground. The planned
1317 separation for each pair is 90 m but this can be changed on orbit by changing the yaw
1318 angle.*

1319

1320 *Figure 3:*

1321 *Comparison of elevation change retrievals from ICESat and ICESat-2. With an
1322 unknown slope Ω and near coincident tracks it is impossible to calculate elevation
1323 change from two single-beam tracks (ICESat; left). ICESat-2 (right) has pairs of beams
1324 that straddle the reference ground track so that its elevation can be extracted through
1325 interpolation of the elevations measured by the two beams.*

1326

1327 *Figure 4:*

1328 *Top: surface roughness, calculated as the RMS difference between elevation*
1329 *measurements and 200-meter linear segments, measured over lower Russell Glacier,*
1330 *Southwest Greenland. The scale is about 100 km horizontal and vertical. Bottom:*
1331 *Height-recovery errors as a function of beam spacing (W) and surface roughness for*
1332 *simulated ICESat-2 data. Roughness values less than 0.5 m are typical of inland ice*
1333 *while larger values reflect surface crevassing.*

1334

1335 *Figure 5:*

1336 *Top: Ice sheet surface slope magnitude for the entire continent of Antarctica,*
1337 *calculated as the 68th percentile of surface slopes for 50x50 km squares on the ice-*
1338 *sheets surface. Bottom, ice sheet roughness calculated as the 68th percentile of the*
1339 *absolute difference between each measured elevation and the average of its two*
1340 *nearest along-track neighbors, for the same grid used for the slope map.*

1341

1342 *Figure 6:*

1343 *Typical ICESat-2-like data from MABEL over the Greenland ice sheet (top), sea ice*
1344 *(middle), and vegetated land surface (bottom). The histograms on the right show*
1345 *photon distributions for the areas between the two red and green vertical lines in the*
1346 *photon clouds. The distance between the lines is 200 m for these examples. In the*
1347 *actual algorithms that are currently being developed for operational processing this*
1348 *distance will be optimized and may vary as a function of signal-to-noise ratio, surface*
1349 *roughness, and number of signal photons.*

1350

1351 *Figure 7:*

1352 *ATLAS clear sky solar photon rate as a function of surface albedo for different Solar*
1353 *Zenith Angles (SZA). Surface is assumed Lambertian. Simulations done with the*
1354 *Discrete Ordinates Radiative Transfer model (DISORT) [Stamnes et al. 1988]. ATLAS*
1355 *parameters used in the calculations include: telescope diameter (0.8 m), field of view*
1356 *(85 μ rad), detector quantum efficiency (0.15), total receiver transmission (0.504) and*
1357 *filter width (0.038nm).*

1358

1359 *Figure 8:*

1360 *Photon densities for a 15 km range in altitude and horizontal distance of about 100*
1361 *km; the brighter the color the higher the photon density. In addition to the surface*
1362 *different types of clouds (PBL stands for “planetary boundary layer”) can be identified.*
1363 *Data were taken with the MABEL instrument on September 21, 2013 over the southern*
1364 *portion of the Chesapeake Bay.*

1365

1366 *Figure 9:*

1367 *Potential range bias error (Rbias) as a function of latitude for the beams that are not*
1368 *monitored by the transmitter echo calibration. This is the residual error after the*
1369 *calibration.*

1370

1371 *Figure 10:*

1372 *Ground track pattern at the equator for the first two years of operation. The bold blue*
1373 *lines show the first tracks for the 2-year period. These are the nominal 91-day repeat*
1374 *tracks. At the equator, the gap is 28.8 km. 91 days later the tracks will be shifted by*
1375 *14.4 km to the right, reducing the gap by half. This halving of the gap will be repeated*
1376 *over two years, i.e. 8 times. The combination of ascending and descending orbits will*
1377 *result in track spacings of less than 2 km. The maximum off-nadir angle is about 1.5*
1378 *degrees.*

1379

1380 *Figure 11:*

1381 *Illustration of one day of ICESat-2 orbits. The blue and red orbit sections indicate*
1382 *where the pointing transitions from the polar “repeat-track mode” to “land/vegetation*
1383 *mode”, respectively. The transition regions have been defined for all 1387 ground*
1384 *tracks and can be updated on orbit.*

1385

1386 *Figure 12:*

1387 *Conceptual mission operations plan. Calibration efforts will be performed over the*
1388 *ocean. TX Echo Calibration refers to Transmit Echo Calibration described in Section*
1389 *3.3. Ocean Scan Measurements are also described in Section 3.3. TX/RX calibration*
1390 *corrects the set point of the control loop that keeps the transmitted beam aligned to*
1391 *the receiver field of view.*

1392